Quantifying the Partition Between Seismic and Aseismic Deformation Along Creeping and Locked Sections of the North Anatolian Fault, Turkey

Maor Kaduri, Jean-Pierre Gratier, Cécile Lasserre, Ziyadin Cakir, Francois Renard

Kaduri, M., Gratier, JP., Lasserre, C. et al. Pure Appl. Geophys. (2018).
https://doi.org/10.1007/s00024-018-2027-2

Quantifying the partition between seismic and aseismic deformation along creeping and locked sections of the North Anatolian Fault, Turkey

Maor Kaduri[1], Jean-Pierre Gratier[1], Cécile Lasserre[2], Ziyadin Çakir[3], François Renard[1,4,*]

[1] Université Grenoble Alpes, Université Savoie Mont Blanc, CNRS, IRD, IFSTTAR, ISTerre, 38000 Grenoble, France

[2] Université de Lyon, UCBL, ENSL, CNRS, LGL-TPE, 69622 Villeurbanne, France

[3] Istanbul Technical University, Department of Geology, Istanbul, Turkey

[4] The Njord Centre, PGP, Department of Geosciences, University of Oslo, box 1048, 0316 Blindern, Oslo, Norway

[*]Correspondence should be addressed to François Renard (francois.renard@geo.uio.no)

Abstract

Shallow aseismic creep is a key deformation component along plate boundaries that contributes to the energy budget during the seismic cycle. Several major active continental faults show spatial alternation of creeping and locked sections. The present study focuses on the evaluation of the aseismic part of the total displacement along the North Anatolian Fault in Turkey. Detailed microstructural analyses of finite strain were performed using various methods, based on change of length or angle, on six representative samples collected over 32 outcrops along locked and creeping sections of the fault. Chemical analyses were used to map mineral composition of fault rocks and to calculate relative volume changes associated with creep. Relationship between finite strain and volume change allowed quantifying the evolution of the penetrative pressure solution cleavage mechanism of creep. In volcanic and analogous creeping rocks, finite strain measurements revealed two spatial scales of strain that correspond to the alternation of two types of shear zones, with cleavages either oblique or sub-parallel to the fault displacement. Using geodetic and geological data, cumulative aseismic displacement was calculated in the range 9 to 49% of the total 80 km displacement in the creping sections, and was negligible in locked sections. The large uncertainty in the kilometer-width creeping sections was related to the difficulty of quantifying high strain values that are associated with high shear displacement and for which measurement uncertainties are large. A promising

way to improve such quantification would be to develop reliable statistical analysis of cleavage orientation in the field.

1. Introduction

Aseismic creep has been extensively documented along several active faults worldwide (Chen and Bürgmann, 2017; Harris, 2017; Bürgmann, 2018). Active fault creep processes develop either as transient (mostly post-seismic) sliding or as permanent sliding. Post-seismic creep rate can evolve through time with various patterns: with an exponential or a power law decay, down to zero or to a residual constant creep velocity (Çakir et al., 2005). In some cases, shallow creep can accommodate the whole tectonic loading as, for example, along the permanent creeping section of the San Andreas fault (Savage and Burford, 1973). In cases where shallow creep only partly releases the tectonic loading, as is the case along the North Anatolian, the Hayward or the Longitudinal Valley faults in Turkey, California and Taiwan, respectively (Çakir et al., 2005, Graymer et al. 2005, Thomas et al., 2014), major earthquakes may still occur at depth and propagate toward the surface.

These contrasting creep behavior patterns may have different implications for seismic hazard assessment. It is therefore crucial to understand the spatio-temporal characteristics of creep and its mechanisms (Bürgmann, 2018). Rock types can partly control fault creep behavior. For example, observations have shown that surface creep rates along the North Anatolian Fault are almost null along fault sections that are rich in massive limestones, but become significant along sections that host various kinds of volcanic rocks that were softened by progressive deformation processes (Kaduri et al., 2017). However, other important characteristics of creep, such as creep deformation duration during a single seismic cycle and over several seismic cycles, as well as the aseismic part of the total displacement during geological fault history, remain to be determined more accurately.

To make progress in understanding creep mechanisms, the displacement associated with creep processes must be evaluated. On one hand, the total displacement over the lifetime of a fault accommodated by both creep and earthquakes can be evaluated by measuring the offset of a number of geological markers (Emre et al., 2013). On the other hand, the displacement associated with creep processes can be deduced only from geodetic or geological strain measurements, quantifying the short-term interseismic strain and the long-term finite strain, respectively. However, surface

geodetic measurements include both the irreversible (ductile creep) and reversible (elastic) parts of the deformation. The distinction between creep and tectonic loading is generally made through simple modeling by considering an elastic half-space surrounding a fault plane (Savage and Burford, 1973; Okada, 1985). In addition, geodetic measurements are representative of slip only in the recent past, covering a few years to several decades. Extending geodetic displacement measurements to the long term (geological times of several millions years) must include an assumption on the variations of the displacement rate with time, which is almost impossible to estimate, especially in areas associating seismic and aseismic processes. Consequently, in order to evaluate only the irreversible part of the large finite strain associated with the creep processes, complementary detailed finite strain measurements in the gouge and damage zone rocks of fault zones are required.

The aim of the present study is to quantify the displacement related to aseismic irreversible creep processes in both creeping and apparently, presently locked sections along the North Anatolian Fault in Turkey. To reach this aim, one needs to measure the associated geological finite strain in both the gouge and the damage zone rocks **(Fig. 1)**. In order to calculate this displacement, two types of data are required: the finite strain values and the width of the zone of associated shear deformation (Ramsay, 1980; Ramsay and Graham, 1970). However, the measurement and the interpretation of such data are rather complex because strain and fault width values evolve with time and along the fault strike during deformation, since the beginning of the formation of the fault to the present day. Strike-slip creeping faults accumulate strain in the upper crust by plastic and viscoelastic mechanisms involving both shear deformation and mass transfer, developing what is known as compaction or dilatant shear zones (Ramsay, 1980; Ramsay and Graham, 1970). In such zones, the mineral composition and rock fabric change due to fracturing, mass transfer, fluid circulation, chemical alteration and metamorphism (Gratier et al., 2013, 2011; Steward et al., 2000; Imber et al., 2001; Jefferies et al., 2006; Collettini, et al., 2009). Moreover, clay gouge comprising low friction minerals such as montmorillonite and saponite also develop (Carpenter et al., 2016; Kaduri et al., 2017; Lockner et al., 2011; Samuelson and Spiers, 2012). In addition, fault growth is not linear with displacement. Power law relationships between maximum displacement and fault width are often reported (Pennacchioni, 2005; Scholz, 2002). At the outcrop scale, irreversible shear strain gradients generally decrease to zero away from the fault over distances of several

centimeters to several kilometers, and sometimes over distances of up to 25 km (Mavko, 1981). The lateral evolution of such strain profiles is often non-linear (Pennacchioni, 2005). The change in shear zone width in time and space thus depends on the deformation mechanisms that combine simple shear, pure shear and volume change and that determine the displacement behavior (Bos and Spiers, 2002; van der Pluijm and Marshak, 2010; Fossen and Cavalcante, 2017). Such heterogeneous shear zones can be classified into three categories based on their width variations: increasing, decreasing or constant in time (Hull, 1988). The shape of displacement profiles across faults depends on whether the deformation process is strain hardening (e.g. deformation diffuses into the host rock) or strain softening (e. g. deformation is localized in narrow zones) (Vitale and Mazzoli, 2008). In particular, strain-softening processes involving simple shear with volume loss are consistent with clay gouge formation (Kaduri et al., 2017).

Measuring and interpreting finite strain and the width of the associated creeping shear from geodetic and geological observations are challenging tasks, especially when deformation involves very high strain values. Despite considerable uncertainties associated with both types of observations, the data presented in this study of the North Anatolian fault can be used to characterize: (i) the spatial correlation between the creep-related strain measured by geodetic methods and that measured by geological methods, (ii) the control of rock lithology on aseismic creep mechanisms and temporal evolution, (iii) the aseismic part of the total displacement on the fault.

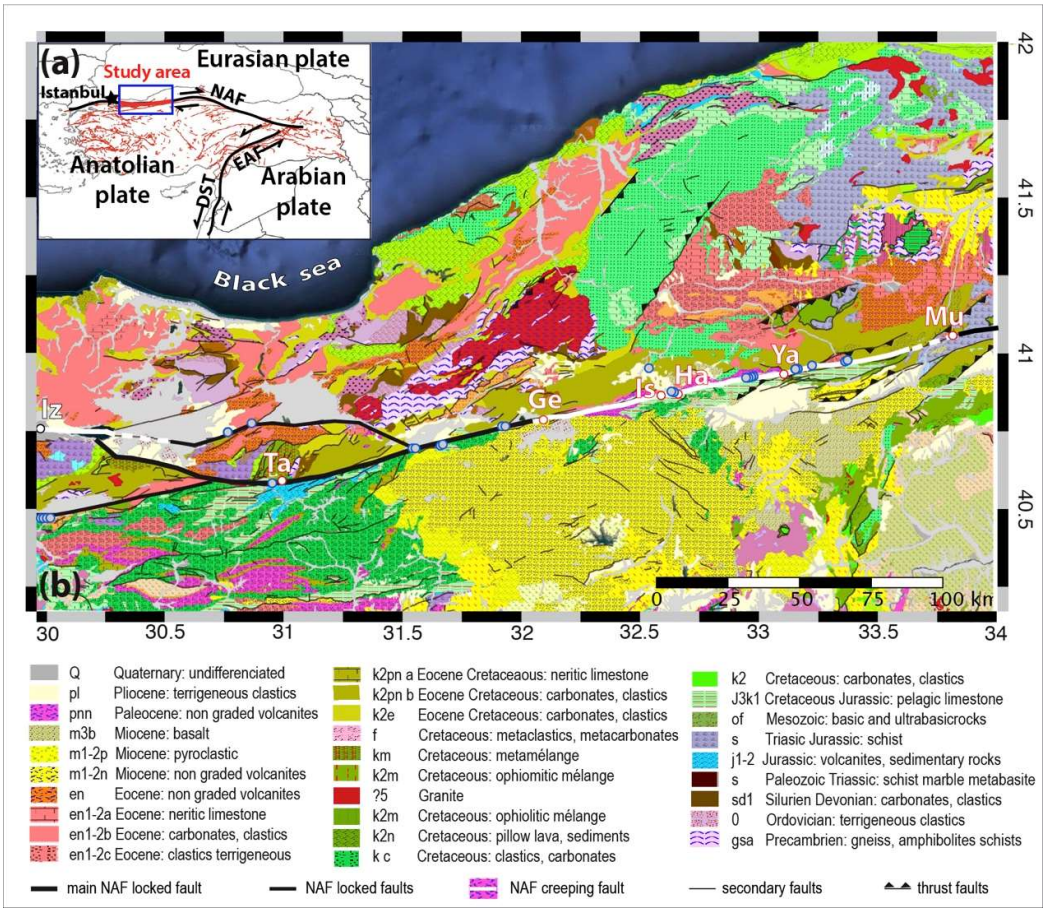

Figure 1. Structural and geological map of the study area along the North Anatolian Fault (NAF), modified from Kaduri et al. (2017). **(**a) Tectonic setting of study area, located east of Istanbul (blue rectangle with NAF in red), adapted from Emre et al., (2013). EAF: East Anatolian Fault, DST: Dead Sea Transform fault. (b) Geological map of the study area with outcrop locations indicated as blue or red circles for the 32 investigated outcrops. Red circles with names locate the six representative outcrops with strain markers described in the present study: Ta=Taskesti (40°34'54.00"N/ 31°1'60.00"E), Ge=Gerede (40°47'3.00"N/ 32°6'30.00"E), Is=Ismetpasa (40°51'55.00"N/ 32°35'41.00"E), Ha=Hamamli (40°52'12.19"N/ 32°39'8.78"E) Ya= Yazioren (40°56'1.59"N/ 33°6'11.09"E), Mu=Mülayim (41°3'5.28"N/ 33°48'17.61"E). The presently creeping segments of Izmit=Iz (west) and Ismetpasa (east) are marked in white (Çakir et al., 2005; Cetin et al. 2014). The locked segments are marked in black. The regional geological map is extracted from an interactive map of the Turkish geological survey (Akbas et al., 2016) available at http://yerbilimleri.mta.gov.tr/anasayfa.aspx. The legend gives the lithology of the formations that are cut by the studied North Anatolian Fault section.

2. Measuring creep-related deformation from fault zone outcrops: setting and approach

2.1 Seismotectonic setting

149 The North Anatolian Fault (NAF) in Turkey is a right-lateral strike-slip plate
150 boundary. This major continental fault accommodates the relative motion between the
151 Anatolian plate, to the south, and the Eurasian plate, to the north. The NAF formed
152 approximately 13 to 11 Ma ago in the east and slowly propagated westward (Şengör,
153 et al. 2004). The long-term geological rate is 20 ±8 mm/yr (Şengör, et al. 2004),
154 consistent with short-term geodetic rates of 24 ±2 mm/yr measured from GPS data
155 (Reilinger et al., 2006) and 25 ±1.5 mm/yr measured from InSAR data (Cetin et al.,
156 2014). The total cumulative displacement along the studied NAF segment (**Fig. 1**)
157 since its initiation is of the order of 80 km (Janssen, et al., 1997; Armijo et al., 1999;
158 Emre et al., 2013; Akbas et al., 2016). A sequence of large earthquakes propagated
159 from east to west and ruptured over ~1000 km of the fault during the 20th century (e.g.
160 Emre et al., 2016), providing evidence of the potential of the fault to accumulate large
161 seismic displacements. However, a striking feature of the NAF is the existence of two
162 slip modes along the fault. Some sections are prone to major earthquakes (Stein et al.,
163 1997) and remain locked in between earthquakes while other sections, well-identified
164 by geodesy measurements, display aseismic creep that possibly initiated as post-
165 seismic slip (Kaneko et al., 2013; Çakir et al., 2014; Cetin et al., 2014) and may
166 behave as a succession of transient creep episodes (Bilham et al., 2016; Rousset et al.,
167 2016). The relative contribution of seismic and aseismic displacement in the 80 km
168 cumulated displacement remains to be evaluated, which is the aim of the present
169 study.
170 At least two sections of the inland part of the North Anatolian Fault have been
171 identified in recent years as aseismic creeping fault sections **(**Ismetpasa and Izmit
172 sections, **Fig. 1)**. Based on an InSAR study of Envisat satellite data along descending
173 orbits, it has been shown by Cetin et al. (2014) that the Ismetpasa creeping section
174 runs from longitude 32.2° to 34.0°, with a maximum horizontal surface creep rate of
175 ~20 mm/yr, located 30 km east of Ismetpasa, and a creeping depth of ~5 km. These
176 results were revised from a new Envisat InSAR analysis including both descending
177 and ascending data, which helped to obtain a better separation of the vertical and
178 horizontal creep components. The Ismetpasa creeping section was found to be longer
179 (running from 31.0° to 35.0°), with two peaks of maximum horizontal creep rate up to
180 ~14 mm/yr, and creep extending down to 9 km depth (Hussain et al., 2016). A clear
181 correlation between shallow creep rate and near-surface fault lithology has been
182 demonstrated (Kaduri et al., 2017): the locked section west of the Ismetpasa creeping

section is mostly composed of massive limestone and dolomite whereas the creeping section is composed of volcanic and ophiolite rocks including clay-rich gouges **(Fig. 1)**.

2.2 Fault sampling and strategy analysis

We calculated the aseismic part of the total displacement along both locked and creeping zones of the North Anatolian Fault. The finite strain and the creeping width for various lithologies were evaluated by investigating 32 outcrops, over a 400 km-long section between the city of Izmit to the west and the eastern end of the Ismetpasa creeping section to the east **(Fig. 1)**. Satellite images and geological maps (Herece and Akay, 2003, Emre et al., 2013, 2016, Akbaş, et al 2016) were used to identify all accessible outcrops following the procedure described in Kaduri et al., (2017). No continuous outcrop was found that would cover the whole kilometer-width of the NAF shear zone. The links and the common features between these dispersed outcrops is that they all show markers of creep deformation associated with the NAF shear zone, either as penetrative cleavage (in volcanic or analogous rocks) or as stylolites (in limestones). So they all attest of the finite aseismic strain, which was associated with the large strike-slip 80 km-displacement of the NAF shear zone during geological times. It must be noted that geological evidence of such creep deformation was found away from the present-day creeping fault, sometimes at more than one-kilometer distance. This observation indicates that the NAF was not a single localized fault during geological times but a kilometer-width shear zone that include several seismic faults and large associated zones of aseismic deformation, an observation consistent with geological maps (Herece and Akay, 2003, Emre et al., 2013, 2016, Akbaş, et al 2016). Building on our first study on the implication of fault rock transformation on aseismic creep (Kaduri et al., 2017), we focus in this following study on the calculation of the total cumulative aseismic displacement from microstructural observations. The main challenge was not only to find outcrops but also to find samples that allow calculating strain values. From the 32 visited outcrops (7 outcrops in the locked segments, 25 outcrops in the creeping segment), 90 oriented hand samples were collected and analyzed in the laboratory and 130 thin polished sections of rock samples were prepared for mineralogical, geochemical and microstructural analyses. All outcrops and samples were chosen to be representative of the wide NAF shear zone and of the geological deformation associated with the

NAF displacement. However, estimating strain values was not possible for all these outcrops and samples. Six representative outcrops with strain markers are presented here, one from the locked section and five from the creeping section **(Fig. 1)**. They represent the various aspects of the strain measurement methods and give a representative focus on the evolution from initial rock to damaged rock and gouges, in order to characterize strain related to aseismic creep.

Strain was measured at various scales from thin section to outcrop scales. Micro- to meso-structural strain measurements were performed on thin sections from millimeter to decimeter scales. Chemical maps were acquired using either X-ray fluorescence spectrometer (XRF, Eagle III) (mm-cm) or Wavelength Dispersive Spectroscopy on an Electron Probe Micro Analyzer (WDS-EPMA) (microns-mm) (Kaduri et al., 2017). Image processing techniques based on MATLAB codes were implemented to calculate internal finite strain from particle distributions or deformation of geological objects. Meso- to macro-structural strain measurements at meter to kilometer scales were derived from field observations and measurements in quarries with outcrops more than 100 m wide, located within the NAF shear zone, of kilometer-width. Due to different deformation markers, two distinct approaches for creeping (volcanic and analogous rocks) and for locked (limestone) sections were used to evaluate the strain values. The techniques are briefly described below including a discussion on the uncertainty of the measurements. These techniques rely on the classical strain analysis procedure well described, for example, in Ramsay (1967, 1980).

3. Strain measurements methodology

3.1 Strain measurements along the creeping section (volcanic and analogous rocks)

The main parameters of the shear zone are defined in **Fig.2a**: the kinematic axes *a* (direction of shear), *ab* (shear plane) and *ac* (displacement plane) and the corresponding coordinate axes *x*, y, and *z*.

Boudinage and folding analysis

Strain values were extracted from XRF chemical maps relying on the difference of composition of the boudins and the veins relative to the matrix. The quadratic

extension/contraction λ is defined as $\sqrt{\lambda} = l_f/l_i$ where l_f is the final length of a deformed object, and l_i is its initial length. The quadratic extension is calculated from boudinage or fractured structures: i) the initial length (l_i) is measured by adding the length of each boudin, and ii) the final length (l_f) is the length from the first to the last boudin **(Fig. 2b)**. The quadratic contractional strain is estimated from folded veins with constant length during deformation by measuring i) the final length l_f of the vein and ii) its initial length l_i as the length of an arc along a deformed object using $l_i = \sum_{i=1}^{n} ds_i = \int_0^{l_0} dx\sqrt{1 + (dy/dx)^2}$, where ds_i is the length of the section between two successive points and can be written as $ds_i = \sqrt{(x_i - x_{i-1})^2 + (y_i - y_{i-1})^2}$ **(Fig. 2b)**.

Uncertainty is linked to the ratio between the resolution of the image and the measured lengths. For the boudinage, the total error is the sum of the errors on the measurements of each boudin element that gives the initial length plus the error on the final length. For the folding, it is the sum of the error on initial and final length. In the following, uncertainties are given with the results and are shown as error bars in the figures.

Volume change due to mass transfer

The relative mass change was estimated by comparing the composition of insoluble and soluble minerals between protected (as undeformed as possible) and exposed (deformed) zones at the micro- to meso-scales within a given shear zone (**Fig. 2c**). The relative mass change is $dm/m = I_p/I_e - 1$, where I_p and I_e are the concentration of all insoluble minerals in the protected and exposed zones, respectively (Gratier et al., 2013). If the rock density does not change, which is the case in the studied samples, the mass change is equivalent to the volume change. In plane strain, the product of the two principal strain values is related to the volumetric change as follows:

$$\sqrt{\lambda_1 \lambda_2} = 1 + \Delta, \quad (1)$$

where Δ is the change in volume (or surface area) (Ramsay, 1967). Because this measurement is based on mineral maps, the accuracy depends on the dimension and on the resolution of these maps. Then, the relative mass change depends on the amount of the insoluble minerals in the protected and exposed zones. An error,

282 defined as a percentage of the calculated volume change or strain, is given in the
283 following. In general, it is smaller than 2%.
284
285 *Grain geometry and orientation analysis*
286 Mineral phases were identified on the chemical maps and the following geometrical
287 properties of individual grains were measured: the minor and major axes of each grain
288 (r_{min}, r_{max}), the grain orientation φ_g defined clockwise relative to the North, and the
289 coordinates of the center of each grain (x_c, y_c) **(Fig. 2d)**. In such cases, the standard
290 deviation of the data is calculated and used to estimate the uncertainty.
291
292 *Fry method*
293 This method is also known as center-to-center method (Fry, 1979, Genier and Epard,
294 2007). The center of every strain marker (e.g. oxide grains) is plotted with respect to
295 the position of all other markers. A plot is built by locating one marker at the origin
296 and by plotting as dots the positions of all other markers. Then another marker is
297 located at the origin and the positions of all other markers are plotted, until all
298 markers have been considered. The result is a cloud of points that contains an empty
299 space (i.e. void) at the origin and which represents the strain ellipse. Strain is
300 quantified using i) the aspect ratio R_{Fry} between the elongation axis (a) and the
301 contraction axis (b) of the strain ellipse; and ii) the angle between the x-axis and the
302 elongation axis also defined as φ_{Fry}. This method is similar to an auto correlation
303 function, which can be used for the same type of object (Heilbronner, 2002;
304 Heilbronner and Barrett, 2014). The normalized center-to-center method (Erslev,
305 1988; Erslev and Ge, 1990) improves the Fry method by taking the grain size into
306 account and was used in the present study. The strain ellipse parameters (R_{Fry}, φ_{Fry})
307 were measured by superimposing all minerals together (**Fig. 2e)**. The actual values of
308 the principal strain axes were then obtained using $R_{Fry} = \sqrt{\lambda_1}/\sqrt{\lambda_2}$ with $\sqrt{\lambda_1} =$
309 $\sqrt{R_{Fry}(1+\Delta)}$ and $\sqrt{\lambda_2} = \sqrt{(1+\Delta)/R_{Fry}}$. Uncertainty derives from fitting an ellipse
310 to the points along the rim of the void in order to extract (R_{Fry}, φ_{Fry}) values. For best
311 fitting higher weights are given to points that are close to the rim while none of the
312 clustered points remain out of the calculation as suggested by Mulchrone (2013). The
313 angle of the ellipse was fixed using the main orientation of the grains. We evaluate
314 the accuracy of this fitting procedure to be $\pm 5\%$.

Cleavage angle evolution within the shear zone

Evolution of the cleavage orientation within shear zone was used to evaluate the displacement (Ramsay, 1980; Ramsay and Graham, 1970) when integrating the volume change (Fossen, & Tikoff, 1993) at millimeter to decimeter scales on thin sections, and up to macro-scale at meter to hectometer scales. In a shear plane, passive line markers (e.g. cleavage or vein) originally making an angle α with the shear zone walls (**Fig. 2f**) are sheared to make a new angle α' (Ramsay, 1980) such that

$$\cot(\alpha') = \frac{\cot(\alpha)+\gamma}{1+\Delta} \quad (2)$$

High γ values are very sensitive to α' angles field measurements: α' values of 1°, 0.5° or 0.1° lead to γ values of 57, 114, or 572, respectively (**Eq. 2**). Consequently, estimating γ from α' is extremely challenging for high strain values, due to the difficulty of measuring α' with sufficient accuracy when it is smaller than 1°. In the following, the uncertainty of this technique is given as the standard deviation of the calculated strains.

3.2 Strain measurements along the locked sections (limestone)

The strain contraction component was calculated by two techniques. The first one involves identifying veins shifted by stylolites (Gratier et al., 2013) and using $\Delta l = l_{v2v}/\tan(\beta)$, where Δl is the thickness of the layer dissolved by the stylolite, l_{v2v} is the distance between the vein walls, and β is the angle between the direction of the vein and the stylolite peaks **(Fig. 2g)**. The initial length of the vein is then obtained by adding the shifted length to the final length of the shifted vein $l_i = l_f + \Delta l$, and the quadratic contraction can be calculated. The second technique involves using the maximum amplitude of the stylolite peaks (Toussaint et al., 2018) and applying: $\sqrt{\lambda_2}_{stylolite}(\varphi) = \frac{L_{Tot}(\varphi)}{L_{Tot}(\varphi)+N_{Stylolite}(\varphi)\cdot\langle Amp_{max}(\varphi)\rangle}$, where $\sqrt{\lambda_2}_{stylolite}$ is the quadratic contraction due to stylolite in their peak direction φ, $N_{Stylolite}$ is the number of stylolites in direction φ, $\langle Amp_{max}\rangle$ is the average maximum peak height in direction φ, and L_{Tot} is the total length of the sample in direction φ. The strain extension component is measured perpendicular to the vein direction. The final length is defined from side to side and the initial length is the spacing between the veins.

Finally, the contraction and extension components are combined and plotted in polar coordinates to define the strain ellipse. Uncertainty is linked to the ratio between resolution of the image and measured lengths. The total error is the sum of the errors on the measurements of shifted veins or stylolites size and on the final length and is given with the results.

3.3 Relation between shear displacement and finite strain values

For simple shear followed by volume change **(Fig. 2f)**, the deformation matrix transforms the undeformed vector (x, z) (initial state) to a new position after deformation (deformed state) (x', z') : $\begin{pmatrix} x' \\ z' \end{pmatrix} = \begin{pmatrix} 1 & \gamma_{s,\Delta} \\ 0 & 1+\Delta \end{pmatrix} \cdot \begin{pmatrix} x \\ z \end{pmatrix}$ where $\gamma_{s,\Delta}$ is the shear strain due to shear and dilation (Fossen and Tikoff, 1993), and the principal strains are:

$$\lambda_{1,2} = \frac{1}{2}\left(1 + \gamma^2 + (1+\Delta)^2 \pm \sqrt{[1+\gamma^2+(1+\Delta)^2]^2 - 4(1+\Delta)^2}\right) \quad (3)$$

where Δ is the volume change. Both the aspect ratio between the principal strain axes $R(\gamma, \Delta) = \sqrt{\lambda_1/\lambda_2}$, and $\theta'(\gamma, \Delta)$ are nonlinear functions of γ and Δ (i.e. surfaces in a three-dimensional coordinate system). Such functions are known as $R - \theta'$ diagrams when plotted together (Fossen and Tikoff, 1993). θ' is the angle between the quadratic extension λ_1 and shear direction. The total shear displacement $d_{\hat{a}}$ is obtained by integrating the shear strain along the z-axis (Ramsay, 1980), (**Fig. 2**)

$$d_{\hat{a}} = \int_0^w \gamma \cdot dz \quad (4)$$

where w is the width of the shear zone, and γ is the shear strain.

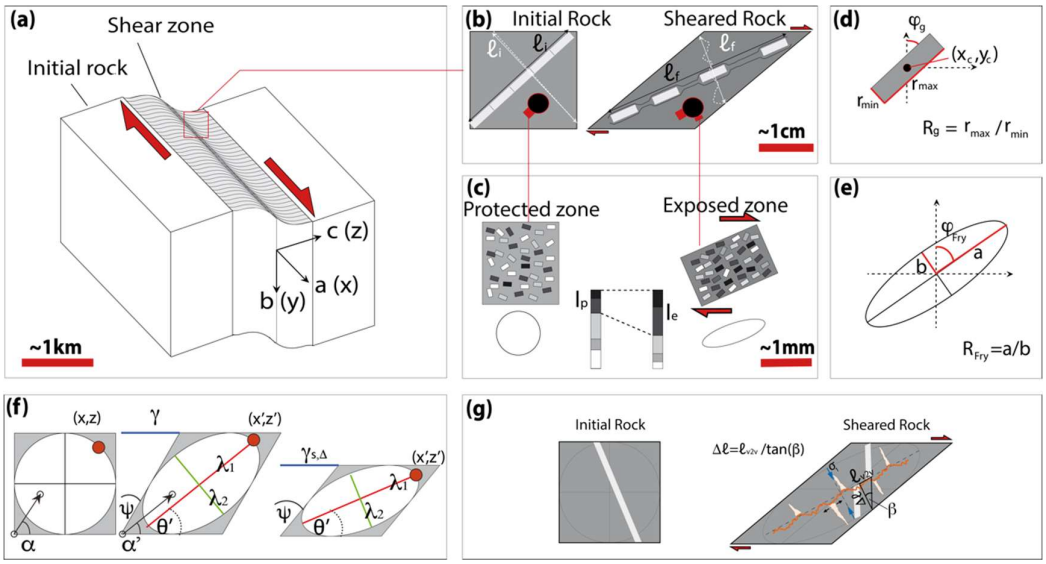

Figure 2. Strain measurements in shear zones. (a) Kinematic axes with *a* the direction of shear, *ab* the shear plane, and *ac* the displacement plane, and corresponding coordinates axes x,y,z. (b) Example of a boudinage strain marker at meso-scale. (c) Magnification of protected and exposed zones with their mineral composition and strain ellipse. (d) Definition of measured parameters of a single grain: major and minor axes r_{min}, r_{max} the aspect ratio R_g and the angle φ_g, and the location of the center of the grain (x_c, y_c). (e) Definition of a strain ellipse using the Fry method with major and minor axes a, b and the aspect ratio between them R_{Fry}=a/b with the angle φ_{Fry}. (f) Schematic deformation in simple shear coupled to volume change, with distortion of a unit circle into an ellipse, adapted from (Ramsay, 1967, 1980). (g) Contraction evaluated from shifted veins along tectonic stylolite.

4. Results of finite strain measurements at selected sites

The structural strain markers differed from one outcrop to another although all were consistent with dextral slip on the North Anatolian Fault. Therefore, the strain values were extracted using different methods, depending on the particular type of strain markers along the shear zones. For five selected sites (Taskesti, Hamamli, Ismetpasa, Yazioren, Mülayim, **Fig. 1**), strain measurements at thin section scale are shown in **Figures 3, 4, 5, 6,** and **7**. For each outcrop, the mineral maps, mineral content histograms, Fry and rose diagrams have a similar color code. For the last selected site, Gerede (**Fig. 1**), strain measurements were integrated at the outcrop and regional scales **(Fig. 8**). Finally, all strain measurements on the six outcrops are integrated in **Figure 9**.

4.1 Taşkesti outcrop (locked section)

The Taşkesti outcrop **(Fig. 1)** exposes the fault zone in massive limestone formations, which are deformed by tectonic stylolites associated with veins as seen in a hand

sample (**Fig. 3**). This sample is well representative of the seven visited outcrops in limestones, which all show several relatively narrow, meter-wide, shear zones with numerous stylolites. The cumulated width of all these narrow shear zones is a few meters at maximum for the whole NAF width. Six thin sections in three orthogonal planes were cut from the Taskesti sample. Two types of tectonic stylolites can be distinguished from the different color of their insoluble residues (either red or black) (**Fig. 3a**). Several generations of veins can be seen that cross cut each other. Some are sub-parallel to the shear fault plane; others are oblique to it. In places, some of the veins are dissolved and shifted perpendicularly to the stylolite plane, indicating the shortening direction. In other places, some of the horizontal veins are stylolitized, while some vertical stylolites are filled with calcite (**Fig. 3b**). **Figure 3c** shows the orientation of maximum amplitude peak directions and stylolite surfaces that are oriented in various directions, with the highest density in the range N70 – N90. It also shows the various orientations of the oblique-to-the fault veins, the most frequent one in the direction N110, and other maximum directions range between N120 and N150 **(Fig. 3c**). This observation is well indicative of the successive generations of stylolites and veins in non-coaxial deformation with alternatively seismic and aseismic deformation.

The total strain was measured from stylolites and veins as follows. Firstly, the extension was measured perpendicular to veins from both the hand sample and thin sections (**Fig. 3a-b**). The strain values obtained from the thin sections were slightly higher compared to the hand sample **(Fig. 3d)**. Secondly, the contraction was quantified by two independent measurements (see **section 3.2**) using: i) shifted veins and ii) stylolite average amplitude. Both methods gave very similar results with a fit of the strain ellipse with $\sqrt{\lambda_1} = 1.2 \pm 0.1, \sqrt{\lambda_2} = 0.9 \pm 0.02$. The main results from these analyses were that, at the decimeter scale, the calculated mass change was $\Delta = 0.08 \pm 0.008$, and the shear strain values calculated from the stylolite values (as only the stylolites are representative of the creep process) led to $\gamma = 0.20 \pm 0.05$ **(Eq. 3)**. It must be noted that, assuming that the shear fault corresponds to the shear direction, the angle of the ellipse with the fault plane, which is about 30°, could indicate higher shear value of about $\gamma = 1.15$. However, in such semi-brittle deformation, it is difficult to evaluate the orientation of the shear direction, which is not always parallel to the fault.

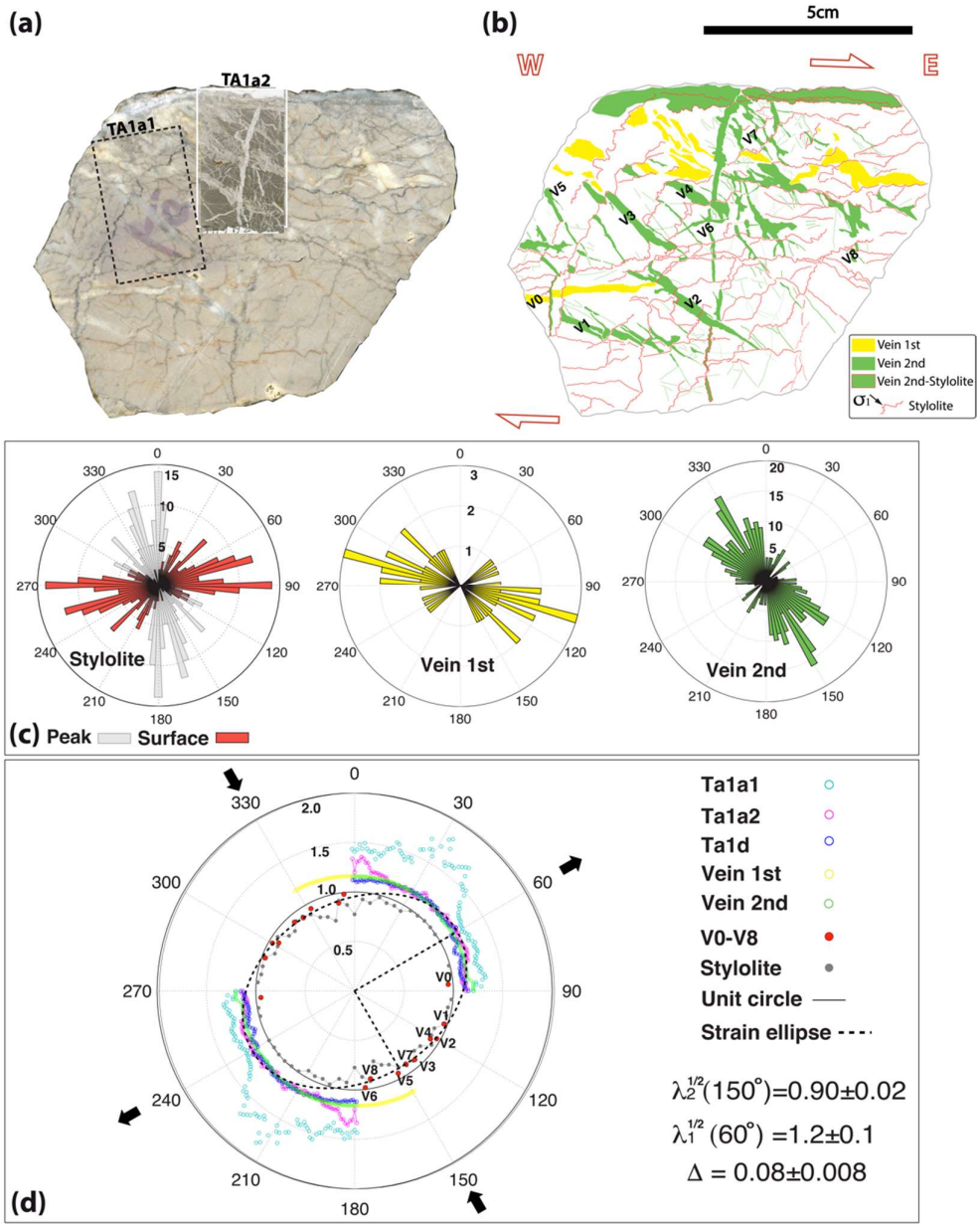

Figure 3. Taskesti outcrop. (a) Limestone hand sample in a horizontal displacement plane (ac, **Fig. 2a**) in the Taşkesti outcrop deformed by tectonic stylolites associated with two families of veins. Locations of the two thin sections Ta1a1 and Ta1a2 are indicated. A third thin-section, Ta1d, is not shown here. (b) Digitized tectonic stylolites and veins. (c) Rose diagrams representing the orientations of the tectonic stylolite surfaces (red) and peaks (gray), and the first and second generations of veins. (d) Strain ellipse based on stylolite and vein data giving contraction and extension values (black arrows), respectively. The locations of individual veins v1 to v8 are given in (b).

4.2 Hamamli outcrop (creeping section)

The Hamamli outcrop **(Fig. 1)** exposes serpentinite rocks deformed by dissolution along cleavage surfaces associated with precipitation in veins (Kaduri et al., 2017). In places, the strain was measured by the alignment of iron oxide minerals that agglomerate sub-parallel to the cleavages. The strain was measured along two planes: a shear plane on the fault (ab) and a displacement plane (ac) (**Fig. 2a)**. The results are presented in **Fig. 4**. The strain values are $R_{Fry} = 2.3 \pm 0.1$ and $R_{Fry} = 3.2 \pm 0.2$ in the shear fault plane (ab) (**Fig. 4a**) and in the displacement plane (ac) (**Fig. 4b**), respectively. Rose diagrams of the iron oxides showed alignments in the strain elongation direction in the displacement plane (**Fig. 4b**) but were slightly oblique to the strain elongation in the shear plane (**Fig. 4a**). This result may be due to the effect of episodic oblique displacements along the fault surface. Because it was not possible to find an area that was less deformed than the studied samples, the mass change could not be calculated. A maximum shear strain value in the displacement plane $\gamma = 1.3 \pm 0.1$ was derived from **Eq. 3** (**Fig. 2f**).

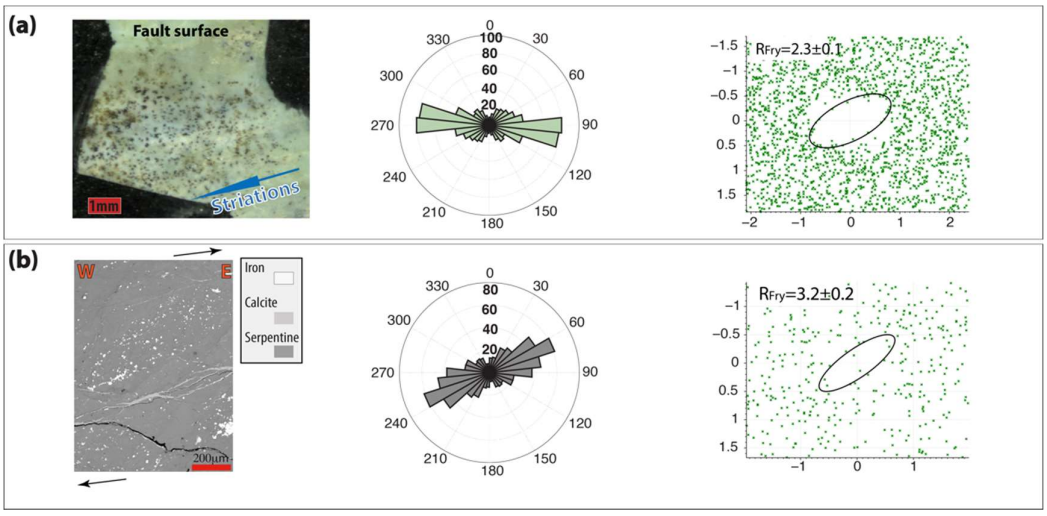

Figure 4. Hamamli outcrop. Serpentine rocks show cleavage-foliation and anisotropic clustering of iron oxide minerals in the cleavage. These microstructures were used to evaluate the strain values in two directions. (a) Strain analysis of a fault surface in vertical shear plane (ab), with the rose diagram of Fe oxides, and plots of the normalized Fry using Fe oxides. (b) Strain analysis with the same two methods in a horizontal displacement plane (ac). The shear arrows are indicative of the sense of shear and do not show an accurate orientation of the shear direction, which is not available on the outcrop where the sample was collected.

4.3 Ismetpasa outcrop (creeping section)

The Ismetpasa outcrop **(Fig. 1)** exposes the fault within volcanic rocks near their boundary with sandstone-shale units. At this site, the deformation in the gouge is associated with tectonic layering leading to more or less fine-grained foliated to granular rocks (F-gouge to G-gouge), **Fig. 5a**. The foliations are deformed around a rigid clast of residual domain of the initial (undeformed) rock. **Figure 5a** shows a digitized horizontal thin section, parallel to the displacement plane (ac) of the shear zone, with four XRF maps of silicon on which the Fry-method analysis gave four R_{Fry} values ranging from 2.7 $\pm$0.1 to 7.5 $\pm$0.4 at centimeter scale (**Fig. 5b**). It was also possible to calculate the strain distribution at millimeter scale within this thin section from six EPMA maps of mineral content acquired in exposed (the most deformed areas) and protected zones (the less deformed area which is the clast of undeformed initial rock), **Fig. 5a**. Some of the maps were masked in order to obtain a more accurate evaluation of localized strain and mineral composition in zones of disaggregated but relatively undeformed large quartzite clasts (map 3, **Fig. 5a**). The relative mass change was calculated excluding magnesite and calcite from the calculation considering that these minerals sealed the porosity of the rock more recently in the deformation process and at least after the process of massive deformation considered here (Kaduri et al., 2017). There was a clear decrease in soluble mineral content from the protected (undeformed) zone to the exposed zones (**Fig. 5c**). Then, in parallel, the strain was measured on these EPMA maps using the Fry method and R_{Fry} values for few representative minerals (albite, anorthite, orthoclase, quartz, smectite). These values were plotted as a function of the relative mass change and showed a near-linear trend (**Fig. 5d**). The values of R_{Fry} converted to quadratic contraction/extension $\sqrt{\lambda_{1,2}}$ using the Δ values **(Eq. 1)**, showed the actual successive change in deformation as a function of the relative mass change **(Fig. 5e)**. Maximum shear strain values are given by maps 2 and 1 with $\gamma = 1.2 \pm 0.1$ and 1.3 ± 0.1 with $R_{Fry} = 7.3$ and 4.5 and with Δ= – 0.66 and -0.3, respectively. The orientation of the grains in the exposed zones was most often aligned with the local foliation. On the contrary, the protected (near undeformed) zones showed random grain distribution with negligible preferred orientation (**Fig. 5f**). It must be noted that the estimated grain orientations and the Fry plots are not parallel, because the calculations are not performed at the same scale and because the deformation is heterogeneous around the clast. The Fry plots are obtained from large XRD maps that

represent a sampling of the whole thin section (area XRF I, II, III, IV) whereas the grain orientation are obtained from local EPMA chemical maps and are located in zones where the orientation of the deformation is pretty the same (area map 1, 2, 3b).

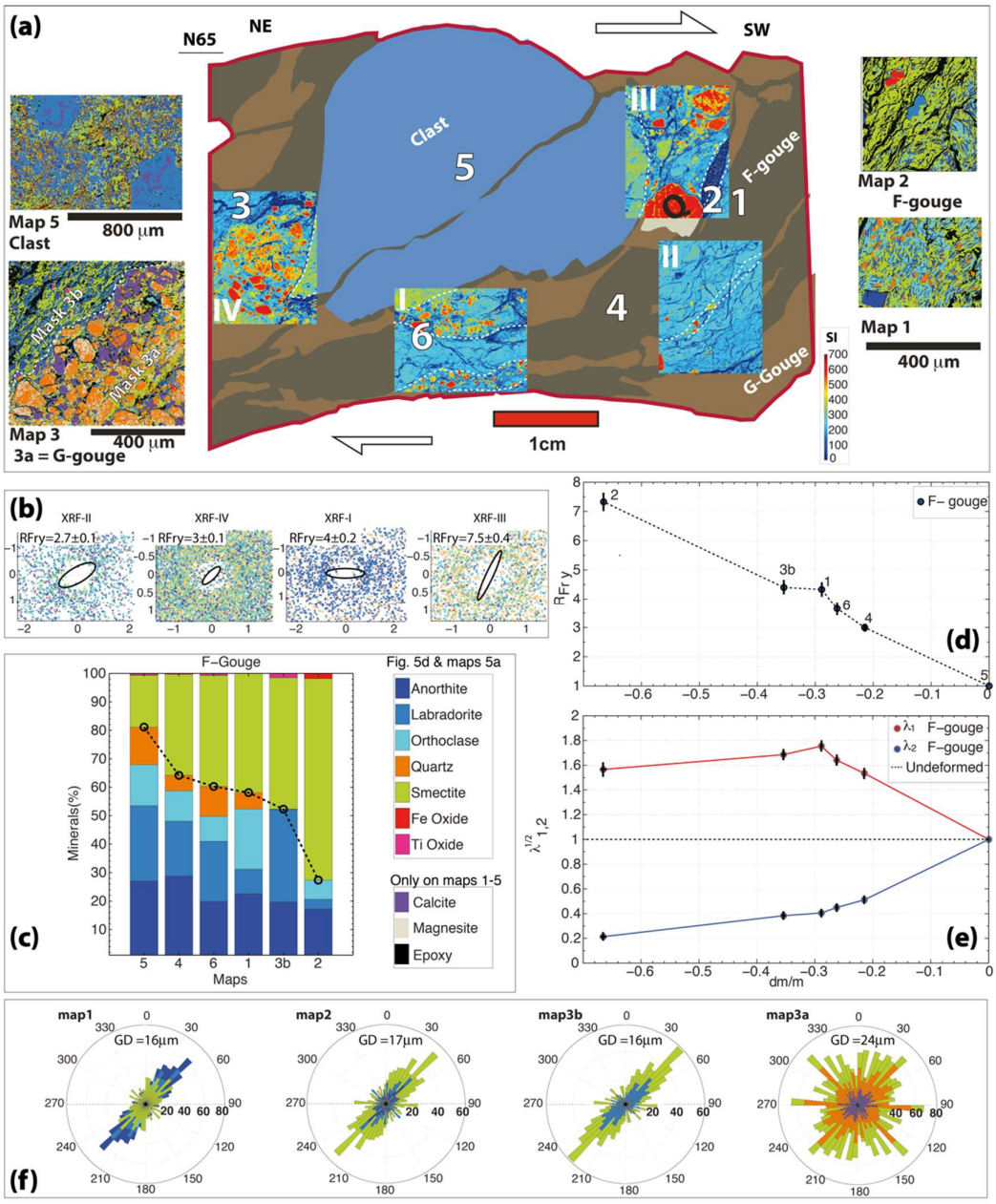

Figure 5. Ismetpasa outcrop. (a) Thin section in horizontal displacement plane (ac) with two types of gouge layers: foliated and granular gouges (F-gouge and G-gouge), around an undeformed clast of initial rock, with four XRF maps of silicon (I-VI, centimeter-scale) and six detailed EPMA maps of minerals located by numbers (1-6, millimeter scale), each corresponds to a different mineral, given in the legend in (c). (b) Fry method based on the four XRF large maps (I-IV) with their location above and using the minerals in the legend in (c). (c) Mineral content of the mineral maps. (d) Strain measurements using the Fry method

and R_{Fry} on these detailed maps plotted as a function of the relative mass change (uncertainty is lower than the symbol size). The reference (protected zones) is map 5 (clast). (e) Plot of the calculated quadratic contraction/extension as a function of the relative mass change. (f) Rose diagrams of grain orientations from mineral maps with mean grain diameters (GD). The color code is the same as in (c). The shear arrows are indicative of the sense of shear and do not show an accurate orientation of the shear direction, which is not available on the outcrop where the sample was collected.

4.4 Yazioren outcrop (creeping section)

The Yazioren outcrop **(Fig. 1**) exposes a shear zone in a mélange of carbonate and volcanic rocks with tectonic layering (rich in alumino-silicates) and carbonate boudinage. A horizontal thin section parallel to the displacement plane (ac) of the shear zone was imaged by XRF in order to segment and measure strain markers. **Figure 6a** shows the calcium XRF map, which emphasizes carbonate boudinage. The strain measurement included two steps. The first step was to measure the quadratic extension $\sqrt{\lambda_1}$ along the preserved boudinage (strain markers 1 to 8 in **Fig. 6a**), which varied in the range 1.4 ± 0.1 - 4.1 ± 0.2. The second step was to measure the deformation recorded in the deformed matrix located near the boudins, using the Fry method on maps of elements acquired from EPMA measurements (location m1-m13, in the Al map **Fig. 6b**). The R_{Fry} values varied from 1.0 ± 0.05 to 4.5 ± 0.2. The plot of these two types of measurement showed a good correlation with a fitted linear regression coefficient R^2=0.89 **(Fig. 6c)**. The relative mass change was calculated using the EPMA maps by comparing exposed and protected zones. **Figure 6d** shows an example of these two types of zones: an exposed zone (map13) and a protected zone (pressure shadow contoured with a dashed line in map2) around a calcite clast. From the protected to the more exposed zones, the mineral assemblage showed a reduction in soluble mineral content and a relative increase in insoluble mineral content (**Fig. 6e**). It is thus possible to calculate the mass change relative to the protected zone **(**map2) **(Fig. 6f)**. There is a near-linear trend between these strain values evaluated by two different methods, $\sqrt{\lambda_1}$ and R_{Fry}, and the mass change **(Fig. 6f)**. Note that such mass change values were only minimum values since the protected zone was not an initial state but rather a less deformed state as attested by the preferred orientation of the grains (**Fig. 6g**). Based on these measurements, boudinage values associated with mean $\Delta = -0.1$ lead to strain ratios ranging from 2 to 19 **(Eq. 1)** and gave a shear strain in the range $\gamma = 1.3 \pm 0.1$ to 4.0 ± 0.2 while the Fry

method gave a range $\gamma = 0.5 \pm 0.05$ to 1.5 ± 0.1 **(Eq. 3).** These values may be compared with the value of $\gamma = 1.3 \pm 0.1$ obtained by the Fry method at the decimeter scale with $R_{Fry} = 2.8 \pm 0.1$ **(Fig. 6h)** and considering a mean value $\Delta = 0.1$. The variation of γ values at millimetric scale indicated the development of parallel-to-the-cleavage differentiated layers with various associated shear values.

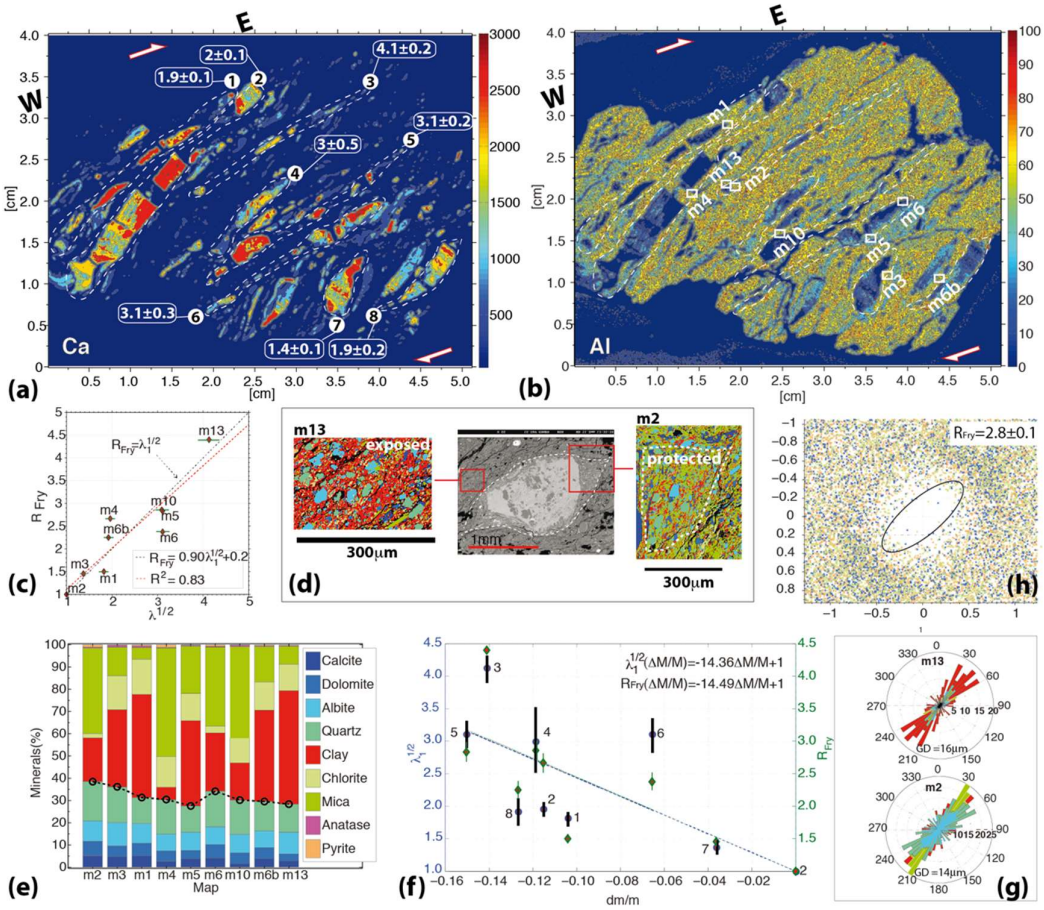

Figure 6. Yazioren outcrop. (a) Calcium map measured by XRF showing boudinage with variation in extensional strain in the horizontal displacement plane (ac). (b) Aluminum map measured by XRF showing the foliation with the locations of the EPMA mineral maps. In (a) and (b) color bars indicate relative content. (c) Correlation between $\sqrt{\lambda_1}$ extension of the boudinage and R_{Fry} of the nearby matrix (with map-numbers). (d) SEM-BSE image and EPMA mineral maps, showing protected (right) and exposed (left) zones. The color-coding for the minerals is given in the legend of (e). (e) Comparative mineral compositions, the dashed line separates soluble (mobile) and insoluble (non-mobile) minerals. (f) Extension values $\sqrt{\lambda_1}$ (from boudinage with numbers) and R_{Fry} (from EPMA mineral maps) versus the relative mass change (uncertainty is lower than the symbol size). (g) Rose diagrams of grain orientations from EPMA mineral maps with mean grain diameters (GD) and orientation with respect to the North. (h) Fry diagram at centimeter scale on the whole thin section from XRF data using the minerals in the legend in (e). The shear arrows are indicative of the sense of

shear and do not show an accurate orientation of the shear direction, which is not available on the outcrop where the sample was collected.

4.5 Mülayim outcrop (creeping section)

In this outcrop **(**see **Fig. 1**), the fault crosscuts a block of ophiolitic mélange embedded into schist, marble and metabasite units. Measurements were performed in the schist that constitutes the main fraction of the rock body. Deformation was measured based on the Fry method at different scales with also the use of folded carbonate veins and the statistical analysis of grain clusters. A horizontal thin section parallel to the displacement plane (ac) revealed a shear zone with cleavage - foliation sub-parallel to the fault and crosscut by carbonate veins in all directions (**Fig. 7a**). The cleavage can be seen on the XRF aluminum map (**Fig. 7b**). Parallel-to-the cleavage and oblique-to-the-cleavage veins registered only a small part of the finite extension $\sqrt{\lambda_1}(0°) = 1.1 \pm 0.02$, and $\sqrt{\lambda_1}(90°) = 1.2 \pm 0.02$, respectively. Contraction perpendicular to the foliation was measured from folded veins giving $\sqrt{\lambda_2} = 0.45 \pm 0.01$ from the decimeter-scale thin section **(Fig. 7a)** to millimeter size EPMA map **(Fig. 7d)** indicating a minimum shear strain γ =1.8 $\pm$0.1 . The deformation evaluated from the Fry method using XRF aluminum maps had a relatively high value $R_{Fry} = 8.5 \pm 0.4$ **(Fig. 7c)**, corresponding to a shear strain γ = 2.6$\pm$0.2. No volume change can be calculated here due to the lack of clear evidence of undeformed (or at least less deformed) protected zones, despite cleavage-foliation being visible with alternating phyllosilicate-rich and albite-quartz-rich tectonic layers indicating significant pressure solution mass transfer **(Fig. 7f)**. Nonetheless, the deformation was highly heterogeneous. Using EPMA maps at millimeter size, some strain variations can be measured when using the Fry method in three different zones: the hinge (H) and the limb (L) of an arcuate structure and an intermediate area (I) **(Fig. 7d)** with R_{Fry} ranging from 1.4 $\pm$0.07 to 4.8 $\pm$0.2 **(Fig. 7e)**. Such strain values, lower at millimeter size than at decimeter scale, implies the existence of some highly localized zones with very high strain values at the sub-grain size. Within these zones, phyllosilicates were oriented sub-parallel to the shear zone with embedded residues of feldspar minerals and Fe oxides **(Fig. 7f)** and such fine-grained thin structures were probably not taken into account well enough by the Fry method.

This problem was investigated by a statistical analysis of the Al grain clusters. More precisely, relying on the detailed observations of the grain orientation and associated

599 Fry ellipses **(Fig. 7d, f, e)**, the distribution of the orientation of elongated grain
600 clusters containing aluminum was fitted with two normal probability density
601 functions. At the decimeter scale **(Fig. 7b)** the cleavage-foliation is overall sub-
602 parallel to the fault at the boundary of the sample. In such ductile context, this fault is
603 presumably parallel to the shear direction and, by measuring the angle θ between the
604 line normal to the fault and the long axis of elongated grain clusters, the amplitude of
605 shear strain is evaluated: the angle between the long axis of elongated grains
606 (assimilated to cleavage plane) and the shear direction (a) is α' when $\alpha = 45°$ (initial
607 cleavage) in **Eq. 2**. This calculation corresponds to the wider normal distribution in
608 **Fig. 7g** that gives an angle α'= 1° associated with γ value of 57. However, at the
609 millimeter scale **(Fig. 7d, f)** we described two types of shear bands: those with grains
610 oblique to the shear direction and those with grains sub-parallel to this shear direction.
611 In order to better constrain the value of the α'angle in the shear bands with grains
612 sub-parallel to the shear direction we choose to concentrate our analysis in these
613 bands (with angles ranging from -5 to + 5° with the shear direction). Doing so we
614 avoid the possible perturbing effect of the grains oblique to the shear. This calculation
615 corresponds to the narrower normal distribution in **Fig. 7g** that gives an angle α'=
616 0.3°. This value of the α'angle is associated with γ value of 190. However,
617 uncertainty on the angle between the normal distribution of the elongated grains
618 cluster and the shear displacement is probably higher than 1°, leading to γ values
619 ranging from 40 to > 200. The coexistence of such a wide range of strain values, the
620 uncertainty of their evaluation and their use to calculate the aseismic displacement is
621 discussed in section **5.2**.
622

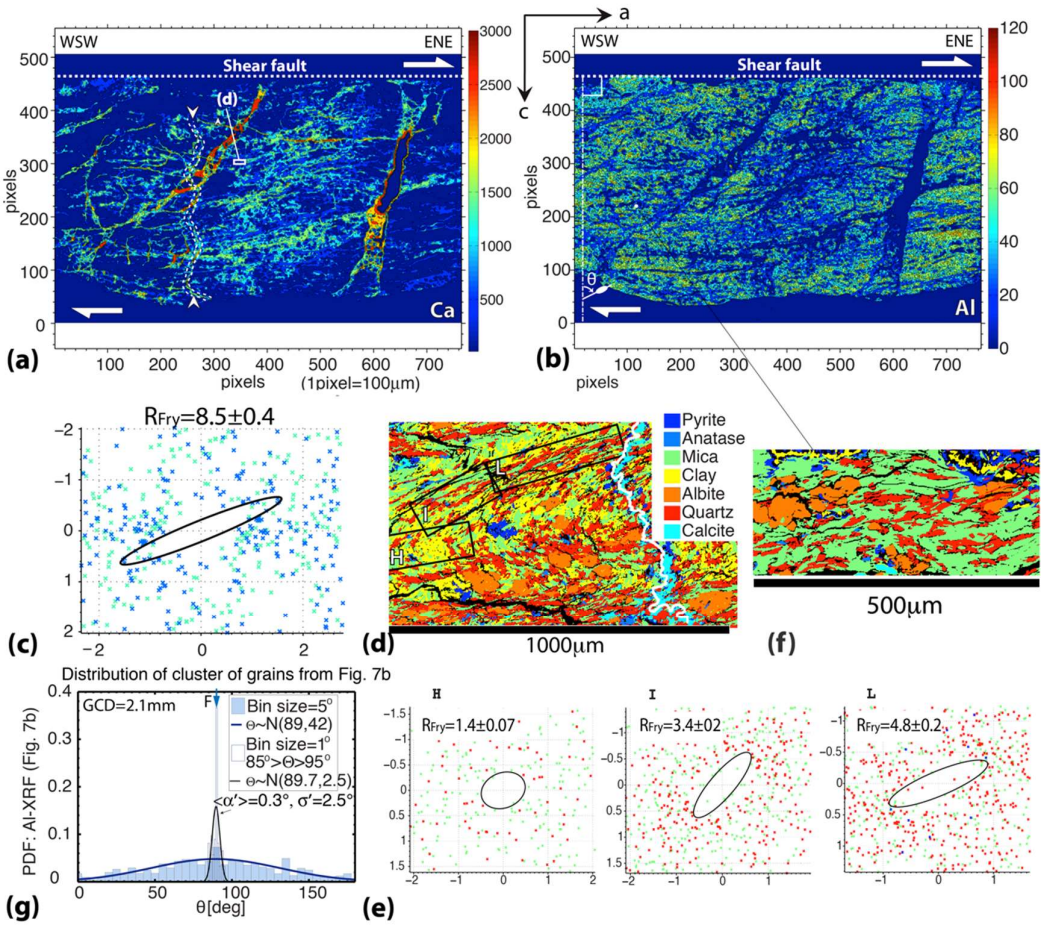

Figure 7. Mülayim outcrop. (a) Calcium map in the horizontal displacement plane (ac) measured by XRF with a folded calcite vein (ptygmatic vein) shown between arrows along dashed white lines. (b) Aluminum map in the same sample indicates sub-parallel cleavage-foliation rich in phyllosilicates. In (a) and (b), color bars indicate relative content. (c) Fry diagram based on XRF-maps (decimeter scale, 7a-b) using the minerals in the legend in (d): anatase and mica. (d) Mineral maps with fold separated by masks in the hinge, the intermediate area and the limb with different cleavage angles (locations are given in **Fig. 7a**). (e) Fry diagram based on the selected zones of the mineral map with increasing values of R_{Fry} from hinge to limb (millimeter scale) using the minerals in the legend in (d). (f) Mineral map in a highly localized deformation zone with sub-parallel to the shear displacement micas and embedded fine-grained quartz. (g) Orientation distribution of clusters of grains containing Al (**Fig. 7b**) fitted by two normal probability density functions (PDF), with the mean diameter of the grain clusters containing aluminum (GCD). Parameters of the two normal distributions are <α'> the mean angle with the fault (F) and σ' the standard deviation: <α'> = 1° and 0.3° and σ'= 42° and 2.5° for the wide and narrow distributions, respectively.

4.6 Gerede outcrop (creeping section)

The Gerede outcrop **(Figs. 1** and **8b**) is an abandoned quarry at the western end of the Ismetpasa creeping segment (Hussain et al., 2016; Cetin et al., 2014). It is located one kilometer south of the present-day active fault zone with several other major strike-

644 slip faults in between mostly buried under Quaternary sediments (Kaduri et al., 2017).
645 The quarry presents a continuous 150 m-wide outcrop (**Fig. 8a**) that reveals a network
646 of 5 to 30 cm thick clay-rich soft gouges with parallel-to-the-fault cleavage-foliation
647 (**Fig. 8a, 8c, 8d**). These faults cross the volcanic units of the Galatia massif
648 (Adiyaman et al., 2001), which are a mélange of dacite, andesite and trachy-basalts
649 (Wilson et al., 1997). These different units are difficult to distinguish. In the gouges,
650 they have been transformed by deformation coupled to low temperature
651 metamorphism (Kaduri et al., 2017). In the damage zones, they have been highly
652 damaged with fractured blocks and dense networks of vertical veins in all directions
653 (**Fig. 8e**). Such sealed fractures were related to episodic inflow events of carbonate-
654 rich fluids that were associated with the successive earthquakes that affected this
655 section of the NAF (Kaduri et al., 2017). Moreover, the deformation was
656 heterogeneous with more or less rigid fractured blocks surrounded by foliated zones
657 with intense deformation displaying a braided fault pattern at all scales, from thin
658 section (**Fig. 5a**) to regional scale (**Fig. 8a**). The size of such rigid blocks decreased
659 drastically in gouges and in zones with cleavage sub-parallel to the shear fault but the
660 boundaries of such zones were undulated and their widths varied along strike (**Fig.**
661 **8a-c-d**). In thin sections, only some islands of volcanic rocks can be seen between the
662 networks of veins. Consequently, it was not possible to evaluate the strain and shear
663 values using particle distribution as in the other studied outcrops.
664 However, it was possible to evaluate the shear values from the angles between the
665 cleavage and the shear fault planes, similar to what was done at microstructural scale
666 for the Mülayim outcrop (**Fig. 7g**). Such angles can be measured either directly in the
667 field or in thin sections. It was not possible to measure the variations of these angles
668 along a continuous path over the entire 150 m of the outcrop. However, the damage
669 zones appeared to be more layered in areas near the gouges than away from them
670 (**Fig. 8c-d**). Thin sections showed that, in these areas near the gouges, the cleavage
671 orientation was sub-parallel to the shear fault plane (**Fig. 8f-g-h**), whereas away from
672 the gouge the cleavage was oblique to the fault (**Figs. 8e)**, as in other outcrops **(Fig.**
673 **5f, 6g**). Such change of cleavage orientation being rather sharp, it was possible to
674 evaluate in the field the width of the shear zones characterized by parallel-to-the-fault
675 cleavage with an uncertainty of about 10%. Such shear zones include all the gouges
676 plus damage zones around them that have the same structural aspect as that seen on
677 thin sections (**Fig. 8f-g**). These shear zones are highlighted in near-transparent white

in **Fig. 8a-c-d** and a cumulative width of 6.0 ± 0.6 m was found along the 150 m width of the quarry. The ratio between this cumulative width of shear zones with parallel-to-the-fault cleavage and the total 150 m width of the outcrop may be evaluated and is equal to 0.04 ±0.004. This ratio can be considered as a representative value at a more regional scale (100-1000 m). The shear strain values associated with cleavage sub-parallel to the fault were not easy to evaluate and will be discussed in section **5.2**. These strain values and the width of the shear zones with fault parallel cleavage were used to estimate the total fault displacement accommodated by creep during geological times in section **5.3**.

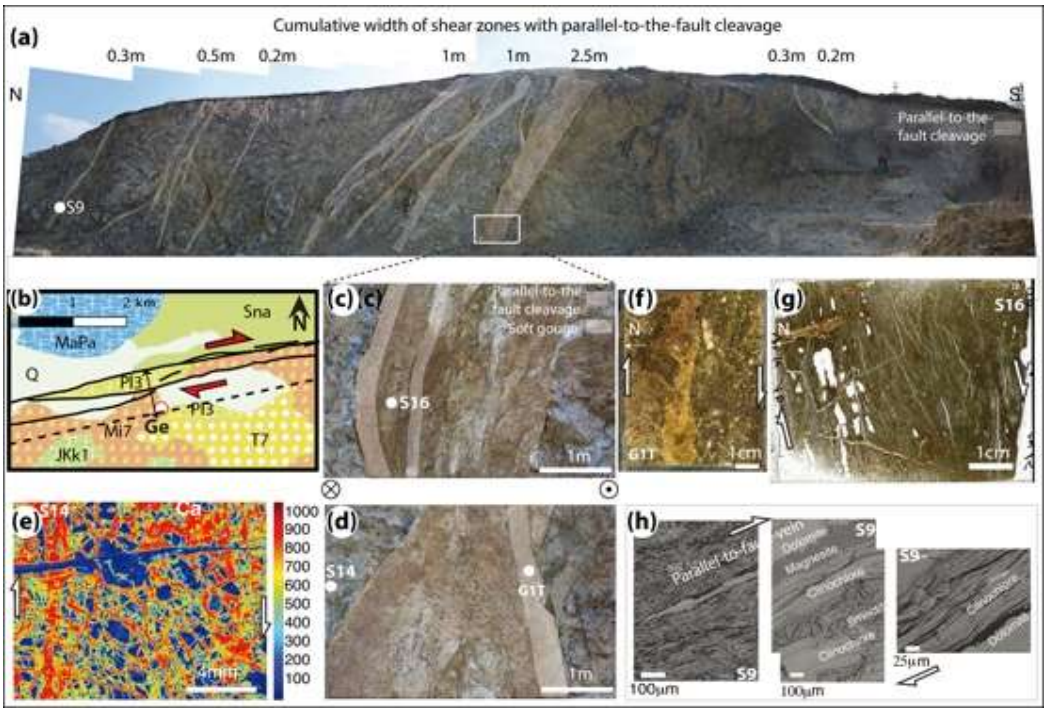

Figure 8. Gerede outcrop. (a) Photograph of the 150 m-wide outcrop showing the fault network and the location and widths of zones (shaded in white) with parallel-to-the-fault cleavage/foliation. (b) Geological map with the trace of the main fault in the outcrop (dashed line), Q=Quaternary, Pl3=Pleistocene conglomerate sandstone, M7=Miocene agglomerate tuff, T7=Eocene andesite basalt, MaPa=Cretaceous limestone, Sna=Cretaceous limestone, JKk1=Jurassic limestone. (c) Zone with parallel-to-the-fault cleavage and soft gouge in the upper part of the quarry: see location in (a). (d) Zone with parallel-to-the-fault cleavage and soft gouge in the lower part of the quarry (not seen in a). (e) Element map of Ca using XRF with typical network of calcite - dolomite veins parallel and perpendicular to the cleavage. The blue perpendicular-to-the-fault vein is a late magnesite vein. (f) Parallel-to-the-fault cleavage in a thin section of soft gouge. (h) Parallel-to-the-fault cleavage in a thin section near the gouge (see location in c). (g) Parallel-to-the-fault cleavage in SEM image with dolomite and magnesite veins parallel to the fault and to the cleavage - foliation (layers of clinochlore and smectite).

5. Discussion

Several parameters are needed to calculate the displacement associated with creep processes in the NAF shear zone: the quadratic extension and contraction strain values, the volume change, that allow calculating the shear strain when data of all outcrops are combined (**Fig. 9**), and the width of the shear zone that allows calculating the shear displacement **(Eq. 4).** The evaluation of these parameters is discussed below, as well as their uncertainty. In section **5.1** we discuss the volume change in the creeping sections and its effect on shear displacement. In section **5.2** we discuss the strain and width evaluation. We evaluate the total displacement in locked sections. We discuss the effect of heterogeneous deformation in creeping sections and we propose a model of two normal shear strain distributions. Finally, the modeling of the total aseismic displacement along the creeping sections is discussed in section **5.3**.

5.1 Volume change evaluation: uncertainty and effect on shear displacement

Here we discuss the relationship between strain and mass-volume change because volume change is an important parameter of the relation between total strain and shear strain (**Eq. 3**). These relations are discussed based on a "strain-ratio/shear-strain/volume-change" diagram (**Fig. 9)**. An horizontal plane strain in 2D is assumed, thereby implying homogeneity along the *y*-axis (Ramsay, 1980; Heilbronner and Barrett, 2014; Fossen and Cavalcante, 2017). For the same measured strain ratio, R, the higher is the volume change the lower is the associated shear strain (**Fig. 9**). For example, for R=10, the shear strain ranges from γ = 2.9 to γ = 2.0 for a volume change ranging from $\Delta = 0$ to $\Delta = -0.5$, respectively **(Fig. 9**). For higher strain ratio, such as R=10000, when cleavage become sub-parallel to the shear zone at less than 0.5° angle, the shear strain ranges from γ = 100 to γ = 72 for a volume change ranging from $\Delta = 0$ to $\Delta = -0.5$, respectively **(Fig. 9)**. Despite such variations of strain for such large variation from $\Delta = 0$ to $\Delta = -0.5$, it does not change the order of magnitude of the shear strain values. It is worth noting that the calculated mass change is a relative value. It is obtained by comparing a deformed "exposed" area with a "protected" area which is either undeformed (in the best case) or which is just less deformed. This is the reason why we also evaluated the deformation of the protected zone from grain geometry and orientation analysis. Moreover, as the rock density does not significantly change, mass change is equivalent to volume change.

As previously discussed in section **2.2**, the six samples presented here are representative of all visited sites along the NAF shear zone (**Fig. 1**): Taskesty in limestone, Hamamli in serpentine and the four other sites (Ismetpasa, Yazioren, Mulayim, Gerede) in various rocks with volcanic origin.

All the sites in limestone show several narrow parallel-to-the-fault shear zones of decimeter width with numerous stylolites. The Taskesti sampling is well representative of all these shear zones for which the deformation near the fault measured at decimeter scale shows no significant volume change with $\Delta = 0.08$ **(Fig. 3)**. Observations (**Fig. 3**) always show clear evidence of alternating seismic (fractures) and aseismic (stylolites) processes (Kaduri et al., 2017). However, the aseismic part remains very low, with mean quadratic values of $\sqrt{\lambda_1} = 1.2 \pm 0.1$ and $\sqrt{\lambda_2} = 0.9 \pm 0.02$ leading to a low shear strain value $\gamma = 0.2 \pm 0.05$, a value not significantly affected by uncertainties on volume change.

At the Hamamli serpentine site, it was not possible to calculate a volume change as no area less deformed than any other was found. This difficulty is a general problem of volume change calculation in serpentine where heterogeneities are rare (Andreani et al., 2005). In Mulayim, the same absence of protected zone prevented us from evaluating the volume change. The corresponding strain values at these sites are then plotted in **Fig. 9** assuming no volume change.

At the other sites, volume change was measured by comparative chemical analyses (**Fig. 5 & 6**) at millimeter scale. These calculations assume that in the deformed areas the soluble minerals dissolve and are removed. A minor part of these soluble minerals, as some feldspars, were transformed into newly crystallized phyllosilicate minerals rather than removed, however, this does not significantly alter the calculations (Kaduri et al. 2017). There is a clear correlation between strain and volume change indicating that the same pressure solution mechanism is responsible for the deformation with the development of parallel-to-the-cleavage tectonic layering. When the protected zone is in an undeformed state, as in Ismetpasa (**Fig. 5**), the volume change varies from one layer to another from 0.22 ± 0.005 to more than 0.66 ± 0.01. When the protected zone is slightly deformed, as in Yazioren (**Fig. 6**), the variations are lower and the uncertainty is much higher. This pattern of successive perpendicular-to-the-compressive-stress layers with various compositions is typical of a pressure solution self-organized process that has been reproduced experimentally

770 (Gratier et al., 2015). This observation was made in the 25 investigated outcrops in
771 volcanic and analogous rocks of the NAF creeping shear zone. It indicates a very slow
772 ductile and aseismic deformation (Gratier et al., 2013). In order to extrapolate this
773 quantitative result to the whole shear zone, some complementary geological
774 observations are needed. No traces of recrystallization of the soluble minerals (quartz
775 and feldspar) are found in the shear zone, so it is likely that the whole shear zone was
776 developed with a decrease of volume at least during the early time of its development.
777 However, later in the NAF development, numerous carbonate veins crosscut some
778 damage zone as seen in Gerede (**Fig. 8e).** As such carbonates need to come from
779 outside since they were not present in the initial rocks, they may have contributed to a
780 local increase of volume. Consequently, in order to evaluate shear strain values
781 representative of the entire NAF shear zone in volcanic and analogous rocks **(Fig. 9)**
782 we used a median regional value of the volume change with a large uncertainty, $\Delta = -0.20 \pm 0.15$.
783
784 Finally, the possibility of much higher volume changes, that we may have missed,
785 must be discussed because large volume change values below $\Delta = -0.8$ have a large
786 effect on the calculation of shear strain (**Fig. 9**). Common observation is that volume
787 change associated with pressure solution is limited to about $\Delta = -0.7$. It is due to
788 several effects especially the progressive decrease of the soluble mineral content and
789 their progressive isolation in the soft matrix of insoluble species that render their
790 stress-driven dissolution more and more difficult (Gratier, et al., 2013). Moreover,
791 there is another effect in shear zones that limits the volume change, which is linked to
792 the rotation of the cleavage. Pressure solution initiates along solution cleavage planes
793 near rigid objects (**Fig. 5a**) and develops progressively further away at 45° from the
794 shearing direction at the beginning of the shearing process. At this stage, the shearing
795 displacement contributes to the tectonic layering process with volume decrease.
796 However, at a later stage with the rotation of the cleavage that becomes sub-parallel to
797 the shear zone, the displacement is less and less dependent on the volume reduction
798 perpendicular to the cleavage. When the cleavage is sub-parallel to the shear zone
799 (**Fig. 7f**), only the effect of the perpendicular-to-the-shear zone compaction
800 contributes to the dissolution. At this stage, large sliding along parallel-to-the-fault
801 cleavage must switch to grain boundary sliding. This mechanism can always be a
802 pressure solution process at grain size scale in order to accommodate relative grain

displacement (Ashby and Verrall, 1973). However, the transfer distance is reduced to the size of the asperities along the grain boundaries. Consequently, the strain rate of such viscous behavior increases significantly for a given stress state (Gratier et al., 2013). This effect contributes to the strain localization parallel to the shear zones. The system can then evolve to a combined frictional and viscous flow behavior (Bos and Spiers, 2002) or can depend only on the friction of individual minerals and on the geometry of their assemblage if mass transfer is no longer possible (Lockner et al., 2011; Sone et al., 2012; Carpenter et al., 2016). In all cases, this effect increases the segregation process between shear zones with cleavage oblique to the shear displacement and shear zones with cleavage sub-parallel to this displacement (**Fig. 10a**). The implication for aseismic displacement estimate is discussed in the next section.

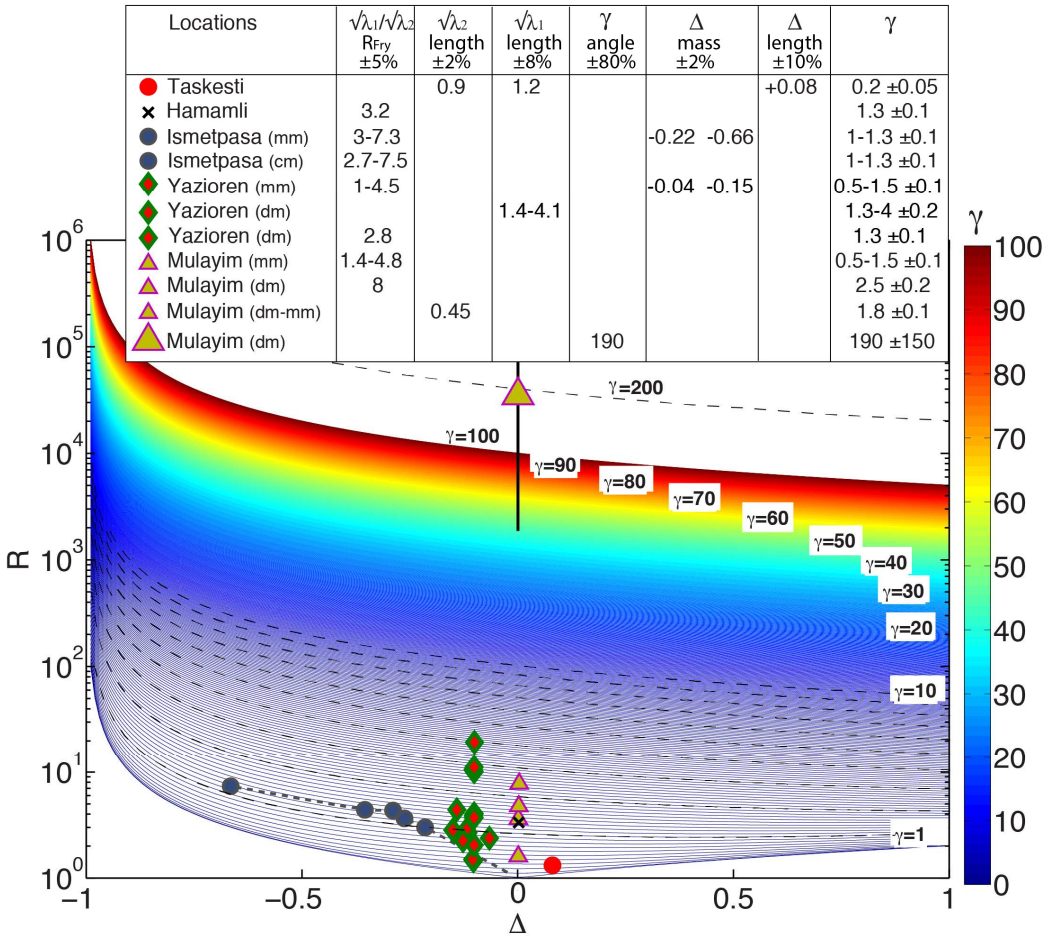

Figure 9. Plot of finite strain and mass-volume change raw measurements from various microstructural methods in the displacement plane (ac). The principal strain axis aspect ratio (R) is plotted versus the relative mass and volume change (Δ) and the

finite shear strain (lines of various colors from γ =0 -blue- to γ =100 -dark red-). Highly contrasted shear strain values γ are found at the Mülayim site, depending on the measurement methods, ranging from 0.5 - 2.5 to 40 - >200 using either Fry method (small triangles) or the angle between cleavage and shear zone (large triangle), respectively. Other symbols refer to sites in **Fig. 3** (Taşkesti), **Fig. 4** (Hamamli), **Fig. 5** (Ismetpasa), **Fig. 6** (Yazioren) and **Fig. 7** (Mülayim). The size of the symbols is larger than the uncertainty except for the high shear strain value deduced from angle measurement where error bars are indicated. Table at top of the figure summarizes strain values at different sites and for different methods: R_{Fry}, measures of length or angle changes, measures of volume changes from chemical content or length changes with mean percentage uncertainty and calculated shear strain values with specific uncertainty. In all cases only the range of values are given for simplicity.

5.2 Strain and width evaluation: uncertainty, heterogeneity and combination of two normal shear strain distributions in creeping sections

Uncertainties on strain measurements have been discussed in the methodological section **3** and are given for each measured value in section **4** and **Fig. 9**. However, such uncertainties are valid for homogeneous deformation. The effect of the heterogeneity of the deformation and the validity of extrapolating measurements from thin sections to the entire shear zone are discussed below and integrated in a normal distribution model of the shear strain, which is used to calculate the aseismic displacement in the next section (**5.3**).

Several independent strain measurements on several different outcrops show the same trend: data are clustered around the same values in **Fig. 9**. However, observation shows variation in measured strain values: the ratio between the principal strain axes (R) ranges from close to 1 in the massive limestone of Taşkesti (**Fig. 3**), to 8.5 (Mülayim, **Fig. 7**) and 7.5 – 19 (Ismetpasa, **Fig. 4**) in volcanic and analogous rocks. The contrasting behavior of the limestone (locked sections) versus the volcanic rocks (creeping sections) has been discussed in another study (Kaduri et al., 2017), and is only briefly summarized here. In the locked sections, using the low shear strain value of $\gamma = 0.2 \pm 0.05$ for the ductile shear zones and their cumulative width of a few meters leads to calculate a total displacement of few meters, indicating that the creep-related displacement in locked sections is almost negligible. This effect is explained by the contrasting behavior of monomineralic (limestone) rocks and polymineralic (volcanic) rocks. Diffusion at the contact surface between two identical grain minerals as in limestone, whose boundaries are most often healed, is much slower than

diffusion at the contact surface between minerals of different nature as in volcanic rocks, where the fluid phase boundary is more continuous (Zubtsov et al., 2004). The difference in behavior is even greater if one of the minerals is a phyllosilicate, which prevents healing (Bos and Spiers, 2000; Zubtsov et al., 2004) or activates dissolution (Renard et al., 2001). This concept that creep deformation is controlled by lithology is supported by a wide range of observations in several major creeping faults (Graymer et al., 2005; Sone et al., 2012; Richard et al., 2014; Thomas et al., 2014; Kaduri et al., 2017).

However, in the creeping sections in volcanic or analogous rocks even at the same site the strain values vary widely, for example from R=1.4 to 8.5 in Mülayim from the Fry method. This strain ratio is even much greater, up to R=10000, when derived from the angles of the cleavage with the shear zone as in Mülayim (**Figs. 7g, 9**). Such heterogeneous pattern is well compatible with the development of the pressure solution layering process discussed in the preceding section (section **5.1)**. Not only the volume change but also the strain values vary from one layer to another in a shear zone. This pattern is schematized in **Fig. 10a.** On the left panel, a sketch of the whole kilometer-width NAF shear zone is presented with several faults and parallel-to-the-displacement shear zones (as in **Fig. 8b)**. In the middle panel, the hectometer scale is displayed with alternating shear zones with cleavage oblique or sub-parallel to the shear displacement (as in **Fig. 8a)**. Finally, on the right panel, we propose a combination of two normal (i.e. Gaussian) shear strain distributions at the scale of the entire NAF shear zone that can be used to evaluate the total aseismic displacement. This model combines (i) a first normal distribution that represents the low strain and wide shear zones with cleavage oblique to the fault zone, with γ_{wsz} and W_{wsz} as maximum shear strain and cumulative width characteristics, respectively, and (ii) a second normal distribution that represents the high strain and narrow shear zones with cleavage sub-parallel to the fault zone, with γ_{nsz} and W_{nsz} as maximum shear strain and cumulative width characteristics. We discuss below how strain measurements on thin sections are extended to regional scale with the associated uncertainties and the evaluation of the cumulative width of these two types of shear zones.

Shear zones with cleavage oblique to the shear displacement

The width of the shear zone W_{wsz} is taken as $2\sigma_{wsz}$, where σ_{wsz} is the standard deviation of the normal distribution. There are few possible measurements of the width of this large zone of shearing. Evidence of several parallel faults indicating kilometer width of deformation is seen on all the geological maps (Herece and Akay, 2003, Emre et al., 2013, 2016, Akbaş, et al 2016) or in Gerede (**Fig. 8b)**, where the presently active fault is located 1 kilometer away from the studied creeping zone. The width $W_{wsz.}$ is thus considered to be at least 1 km-wide. Another kilometer-width value can be obtained from the modeling of geodetic data (see section **5.3**).

Uncertainty on strain measurements assuming homogeneous deformation is rather low (see table **Fig. 9**). However, heterogeneity is everywhere, amplifying the uncertainty. The normal distribution model implies to choose the highest value of the shear strain γ_{wsz} that is representative of the zones with oblique cleavage **(Fig. 10a)**. For a kilometer-width normal distribution, samples for such a γ value representing some meters in size seems realistic. We did not perform strain measurement at this scale but we will consider that measurements on large thin sections at decimeter scale are representative of this meter scale. The higher strain values at thin section scale are from Mulayim and Yazioren sites. The use of the Fry method gives a strain ratio R = 8.5 $\pm$0.4 in Mulayim leading to $\gamma = 2.6 \pm 0.2$ **(Fig. 7c).** This value is a minimum due to the limitation of the method to evaluate high strain values, because of the difficulty of measuring a very elongated elliptical void in cloud of points. In Yazioren, it is possible to compare two different methods: boudinage measurements give shear strain values in the range $\gamma = 1.3 \pm 0.1$ to 4.0 ± 0.2, whereas the Fry method gives $\gamma = 1.3 \pm 0.1$ **(Fig. 6)**. The two methods do not rely on the same markers and the heterogeneity of the deformation with undeformed truncated blocks and highly localized deformation is probably not well accounted for by the Fry method. The boudinage measurement is also limited because with large extension it is difficult to link the truncated blocks. Moreover, the boudinage measurement distributions should also be discussed. As for extension deduced from truncated belemnites (Ramsay, 1967), one can either consider that the truncated objects were heterogeneously fragmented in homogeneous deformation and then the maximum extension values are the most representative of the whole deformation, or consider that the deformation was heterogeneous and a mean value is best representative of the whole deformation (Gratier et al., 2013). Here, as we clearly see heterogeneous shear deformation at all

scales it seems more realistic to take a mean value of the boudinage measurement of $\sqrt{\lambda_1} = 2.6$, leading to a shear strain of about $\gamma = 2.4$ (with $\Delta = -0.1$), close to the value $\gamma = 2.6 \pm 0.2$ (with $\Delta = 0$) measured in Mulayim. These values must be mitigated by the effect of the volume change ($\Delta = -0.2 \pm 0.15$) as discussed before (section **5.1**), leading to a range of shear strain of $\gamma_{wsz} = 1.9 - 2.7$ that will be used in section **5.3**.

Shear zones with cleavage sub-parallel to the shear displacement

Zones of cleavage sub-parallel to the shear displacement are revealed at thin section scale by two types of observations. The first one results of the statistical analysis of the orientation of elongated cluster of grains, for which the long axis can be assimilated to cleavage planes, that shows normal distribution with very low angles with the shear plane ($\alpha' = 0.3°$), see **Fig. 7g**. Another key observation is that the shear strain values deduced from particles and length change measurements are sometime higher at decimeter scale than at millimeter scale **(Fig. 7)**. This observation implies the existence of some highly localized zones with very high strain values associated with cleavage sub-parallel to shear displacement **(Fig. 7f)** that cannot be captured by such measurements. At regional scale, as shown in the Gerede outcrop, there are clear evidences of zones with cleavage sub-parallel to the main shear zone displacement among zones with cleavage oblique to the shear displacement **(Fig. 8)**. These intensively deformed zones include gouges but also some parts of the damage zones that show cleavage planes sub-parallel to the shear zone **(Fig. 8f-g)**. The ratio between the widths of shear zones with parallel-to-the-fault cleavage and the total width has been evaluated in the range 0.04±0.004. This value can be considered as a representative value at a regional scale (100-1000m). This ratio is used to evaluate the cumulative width of the narrow zones for example $W_{nsz} = 40 \pm 4$ m for a total width of 1km.

Regarding the reliability of the strain measurements in order to evaluate the maximum value of the normal distribution of the shear strain values, γ_{nsz}, as before, for a kilometer-width normal distribution samples representing some meters in size seem realistic. We used measurements on large thin sections at decimeter scale as representative of meter size. The statistical analysis made in the Mulayim thin section gives a value of $\gamma_{nsz} = 190$ associated with an angle $\alpha' = 0.3°$ with the shear

displacement. However, uncertainty on the angle between the normal distribution of the elongated grains cluster and the shear displacement is probably higher than 1°, leading to γ_{nsz} value ranging from 40 to > 200 (see section **4.5**). Using such large uncertainty in the displacement calculation is very difficult, whereas choosing some arbitrary values does not seem realistic either. Moreover we must also integrate the fact that we were not able to evaluate the volume change in this thin section due to the lack of protected zones representative of initial state, despite observations of mass transfer, so we took $\Delta = 0$. But according to other measurements as in **Fig. 5d** it is likely that the volume change in the shear zones with cleavage sub-parallel to the displacement must be very large, up to $\Delta = -0.6$. With such large volume change the shear strain value of 190 decreases down to near 100 **(Fig. 9)**. So we finally choose $\gamma_{nsz} = 100$ as a conservative representative order of magnitude. Then, after integrating all the other parameters with lower uncertainty in the modeling to calculate the total displacement, we will be able to evaluate more precisely the possible range of the shear strain values γ_{nsz} in the zones with cleavage sub-parallel to the shear displacement.

5.3 Calculation of the aseismic part of the total displacement along creeping sections of the North Anatolian Fault

In this section, the relative contribution of aseismic displacement to the total cumulative displacement, along creeping sections of the NAF, is estimated. At the continental scale, rocks deform both by reversible deformation (elastic tectonic loading) and by irreversible deformation (ductile or brittle) that involves plastic dissipative processes and that depends on the system size (Karmakar et al., 2010). We propose to use of a combination of geodetic and geological data in order to evaluate the width of the creeping zone, that we combine with shear strain measurements at the outcrop scale to estimate the aseismic part of the total displacement on the fault (Ramsay, 1980) **(Eq. 4)**.

5.3.1 Modeling creep behavior at the present time

Geodetic data used in this section are horizontal surface velocity maps across the NAF taken from the InSAR time series analysis of Cetin et al. (2014). These maps are

based on Envisat satellite data acquired between 2003 and 2010. Horizontal velocity profiles perpendicular to the fault were extracted from these maps and modeled using:

$$V(z) = \frac{S}{\pi} arctan\left(\frac{z}{d_1}\right) + C\left(\frac{1}{\pi} arctan\left(\frac{z}{d_2}\right) - H(z)\right), \quad (5)$$

where z is the distance perpendicular to the fault. Equation **5** is derived from the classical model of a dislocation into an elastic space of Weertman and Weertman (1964) and Savage and Burford (1973). This equation models surface horizontal velocities V across a strike slip fault locked from the surface to a locking depth d_1 and sliding at the tectonic loading rate S below (first term of the equation). It was modified to take into account creep at velocity C from the surface down to a depth d_2 (second term of the equation), as in Hussain et al. (2016). This second term of the equation including the Heaviside step function H thus represents the expected velocity step across fault due to shallow creep.

The corresponding shear strain rate $\dot{\varepsilon}_{xz}$ along the profile is the spatial derivative of the velocity profile:

$$\dot{\varepsilon}_{xz} = \frac{\partial V(z)}{\partial z} = \frac{S}{\pi} \cdot \frac{d_1}{d_1^2+z^2} + C\left(\frac{1}{\pi} \cdot \frac{d_2}{d_2^2+z^2} - \delta(z)\right) \quad (6)$$

where x is the distance along the fault and z along the width of the shear zone (see the coordinate system in **Fig. 2a**).

Figure 10 b-c shows the theoretical surface velocity profiles expected across a fault that: i) slides at a rate of 20 mm/yr below 15 km (tectonic loading) and is locked above, ii) creeps between the surface and a depth of 2 km at a rate of 10 mm/yr and is locked below between 2 km and 15 km, iii) combines both slip processes. These values correspond to the averaged values of the tectonic loading rate (20 mm/yr), locking depth (15 km), creep rate (10 mm/yr) and depth of creep (2 km), at the longitudes of Ismetpasa and Hamamli sampling sites along the creeping section of the NAF. The first two parameters (tectonic loading rate and locking depth) are based on GPS measurements (Reilinger et al. 2006). The last two (rate and depth of creep) are from the creep rate distribution model shown in figure 9 of Cetin et al. (2014) (from inversion of InSAR data). The corresponding theoretical strain rate profiles are also derived in **Fig. 10d**.

Figures 10e-f show two horizontal velocity profiles derived from Cetin et al. (2014), perpendicular to the fault (30 km-wide and 240 km-long), and intersecting it at the Ismetpasa and Hamamli sites. Data are corrected from the tectonic loading at depth, from (Reilinger et al. 2006), so that the profiles correspond only to the shallow creep

signal. Superimposed on these profiles are models from Cetin et al. (2014), with similar parameters as for **Fig. 10b-c** (black lines on **Fig. 10e-f** are computed from the right-hand term of **Eq. 5** considering only shallow creep). The creep rate is considered to be uniform from the surface to a given depth (10 mm/yr down to 2 km depth). Given that the tectonic loading rate is about 25 mm/yr on average for the entire North Anatolian Fault (Reilinger et al., 2006; Cetin et al., 2014) and 20 mm/yr near Ismetpasa (Cetin et al., 2014), the present-day shallow creep accommodates about 40-50% of the tectonic loading.

These models on **Fig. 10e-f** are derived to obtain shear strain rate profiles **(Fig. 10g)** at the sampling sites in order to:

1) Evaluate the relevance of the proposed combination of two normal (i.e. Gaussian) shear strain distributions (**Fig. 10a)**.

2) Calculate the width of the wide shear zone in the past assuming that it keeps the same width (at least the same order of magnitude) throughout the deformation process.

We propose to fit the geodetic strain rate model of **Fig. 10g** (green curve) at Ismetpasa and Hamamli with a superposition of two normal distributions representing the cumulative width and shear strain associated with both types of shear zones (e.g. damage and gouge zones in the present time). The shear components can be approximated with normal distributions $\gamma \sim N(0, \sigma^2)$ so that:

$$\gamma(z) = \sum_k \gamma_{0,k} \cdot e^{-z^2/2\sigma_k^2} \quad (7)$$

where γ is the shear strain, and index k refers to the type of shear zone. The width of the shear zone is considered to be $W_k = 2\sigma_{\mathrm{k}}$. Postulating that the shear strain is the only time-dependent variable $\gamma(t)$, the shear strain rate $\dot{\gamma}$ obtained by deriving **Eq. 7** over time is $\dot{\gamma}(z) = \sum_k \dot{\gamma}_{0,k} \cdot e^{-z^2/2\sigma_k^2}$.

Considering that strain rate and width values are independent for the damage zone and the gouge zone, the strain rate and width of the damage zone are first inverted: $\dot{\gamma}_d = 1.6 \cdot 10^{-6} yr^{-1}$, and W_d = 4.4 km, respectively (**Fig. 10g,** orange normal distribution). This value of several kilometers for the width of the damage zone is consistent with the kilometer scale fault zone width observed in the field (**Fig. 8b**). Owing to the low resolution (pixel size 20 m east-west, 4 m north-south) and high noise level (**Fig. 10e-f**) of InSAR satellite data it is not possible to provide a strain rate model in the fault near-field that is sufficiently precise to estimate the width of the gouge zone properly.

This width is therefore taken as W_g=1 m, based on field measurements from Kaduri et al. (2017). The strain rate of the gouge zone is finally estimated as follows. The cumulative displacement rate along a fault, $\dot{D}$, is given by the integration of the two normal distributions over a z-axis perpendicular to the fault plane, in a range $(-\infty, +\infty)$ (placing **Eq. 7** in **Eq. 4**):

$$\dot{D} = \dot{\gamma}_g \cdot \int_{-\infty}^{\infty} e^{-z^2/2\sigma_g^2} dz + \dot{\gamma}_d \cdot \int_{-\infty}^{\infty} e^{-z^2/2\sigma_d^2} dz$$

$$= \dot{\gamma}_g \cdot \sigma_g \cdot \sqrt{2\pi} + \dot{\gamma}_d \cdot \sigma_d \cdot \sqrt{2\pi} \quad (8)$$

Assuming that $\dot{D}$ is 10 mm/yr based on the InSAR analysis of Cetin et al., (2014), **(Fig. 10c-d)**, and given the values of $\dot{\gamma}_d$ and W_d obtained above, it is estimated that $\dot{\gamma}_g = 0.89 \cdot 10^{-3}\ yr^{-1}$ from **Eq. 8,** with $W_k = 2\sigma_k$. It is worth noting that this partition of the displacement rate between damage zone and gouge is strongly dependent on the imposed width of the gouge, and significant detailed improvements of this partition would rely on a better spatial definition of present-day geodetic measurements. However, this formalism has the merit of representing in a consistent framework both structural geologic and geodesic data, which have different spatial and temporal scales.

5.3.2 Modeling the creeping behavior in the past since the beginning of fault sliding

As discussed in section **5.2**, two types of strain distributions must be taken into account when calculating the displacement associated with creep processes since the beginning of fault sliding (**Fig. 10a**). Firstly, a normal distribution represents the low strain and wide shear zones with cleavage oblique to the fault zone, with γ_{wsz} and W_{wsz} as maximum shear strain and width characteristics, respectively. Secondly, another normal distribution represents the high strain and narrow shear zones with cleavage sub-parallel to the fault zone, with γ_{nsz} and W_{nsz} as maximum shear strain and width characteristics, respectively. Based on geodetic data the width of the wide shear zone W_{wsz} is evaluated to be 4.4 km (**Fig. 10g**). As discussed in section **5.2**, geological observations near Gerede lead to a minimum width of the fault zone of 1 km (**Fig. 8b**). Strain measurements on field samples give shear strain values ranging from $\gamma_{wsz} =$ 1.9 to 2.7 when integrating the uncertainty on strain measurements and volume change at the scale of the NAF shear zone (see section **5.2**). For the narrow

shear zones, as discussed in section **5.2**, the width of the narrow zones can vary from 0.036 x 1000m = 36 m to 0.044 x 4400m = 194 m and a conservative value of γ_{nsz}= 100 is used for the shear strain (see section **5.2**). All these strain and width values can be used to evaluate the limits on the total displacement associated with aseismic creep, by integrating the shear strain values of the two normal distributions across the fault. The maximum and minimum aseismic displacement is calculated using **Eq. 8** with γ instead of $\dot{\gamma}$. The maximum displacement results from the combination of the maximum displacement associated with the low strain and wide shear zones (using the maximum values $\gamma_{wsz} = 2.7$ and W_{wsz} = 4.4 km, (corresponding to σ_{wsz}= 2.2 km), which is 15 km, and of the maximum displacement associated with the high strain and narrow shear zone (maximum values $\gamma_{nsz} = 100$ and W_{nsz} = 194 m (corresponding to σ_{wsz}= 97m), which is 24 km, leading to a total maximum displacement of 39 km. Similarly, the minimum displacement is estimated using the minimum values of γ_{wsz} and W_{wsz} for the low strain and wide shear zone ($\gamma_{wsz} = 1.9$; W_{wsz} = 1 km), giving 2.4 km of displacement, and the minimum values of γ_{nsz} and W_{nsz} for the high strain and narrow shear zone ($\gamma_{nsz} = 100$; W_{nsz} = 36 m), giving 4.5 km of displacement, leading to a total minimum displacement of 6.9 km. The estimated total aseismic displacement thus ranges between 9 % and 49 %, of the total shallow displacement of 80 km during geological times.

The conservative value γ_{nsz} = 100 can now be discussed in relation with geological observations. Using shear strain values of $\gamma_{nsz} = 200$ for the zone with cleavage sub-parrallel to the shear displacement would mean that nearly 80% of the total displacement was accommodated by aseismic creep, which seems a maximum since we see evidence of earthquakes all along the NAF deformed zone. Using shear strain values of γ_{nsz} less that 70 would mean that the zones with cleavage sub-parallel to the shear zone accommodated less displacement than the wide zones, which seems rather unrealistic. Consequently, these two shear strain values may be considered as upper and lower bound of the shear strain values in zone with cleavage sub-parallel to the shear displacement.

From a more general point of view, this type of calculation reveals the difficulty in quantifying large displacements along regional shear zones. Measurements based on length changes are limited to shear strain below 2.5 to 4, depending on the methods. Measurements based on angle changes are much more efficient but they need to be

done with reliable statistical analysis that still need to be developed on the field with numerous cleavage measurements, which was not possible to do here because of the quality of the outcrops.

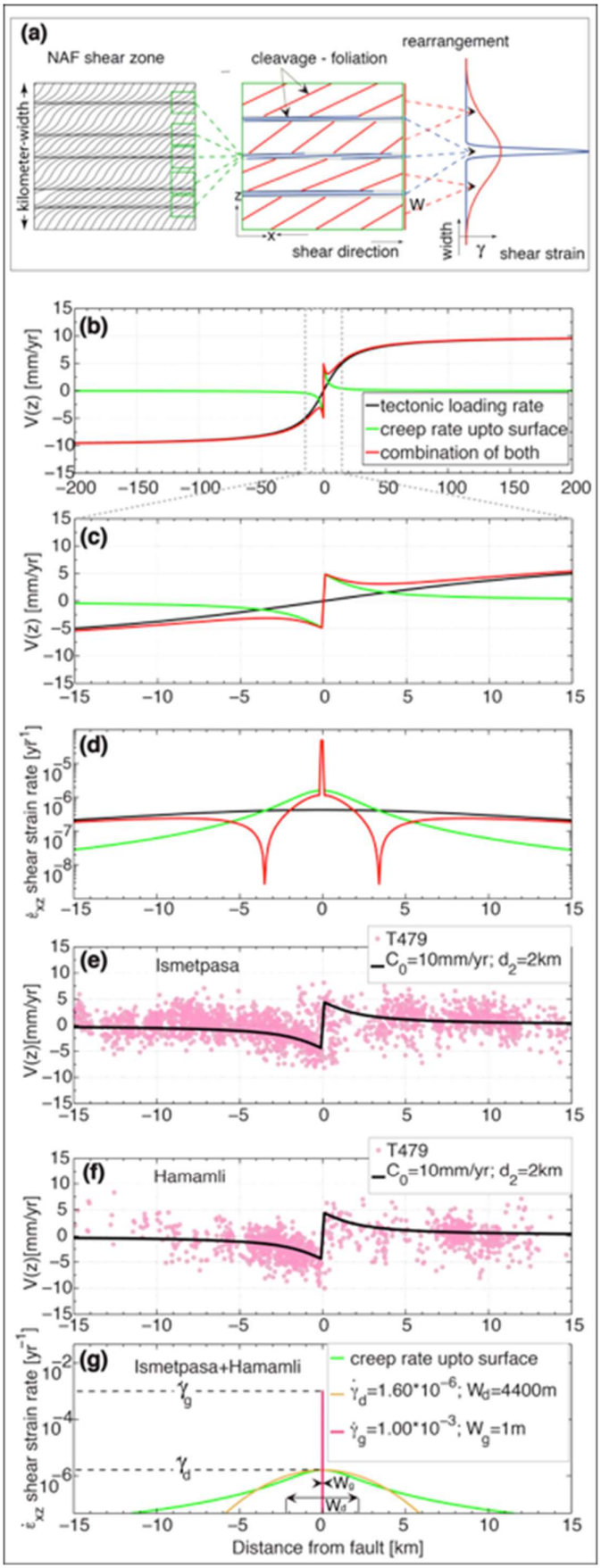
(a)
NAF shear zone
cleavage - foliation
rearrangement
kilometer-width
z
x
W
shear direction
width
γ
shear strain
(b)
V(z) [mm/yr]
tectonic loading rate
creep rate upto surface
combination of both
(c)
V(z) [mm/yr]
(d)
$\dot{\varepsilon}_{xz}$ shear strain rate [yr^{-1}]
(e)
Ismetpasa
T479
C_0=10mm/yr; d_2=2km
V(z)[mm/yr]
(f)
Hamamli
T479
C_0=10mm/yr; d_2=2km
V(z)[mm/yr]
(g)
Ismetpasa+Hamamli
creep rate upto surface
$\dot{\gamma}_d$=1.60*10^{-6}; W_d=4400m
$\dot{\gamma}_g$=1.00*10^{-3}; W_g=1m
$\dot{\gamma}_g$
$\dot{\gamma}_d$
W_g
W_d
$\dot{\varepsilon}_{xz}$ shear strain rate [yr^{-1}]
Distance from fault [km]

1121

Figure 10. Aseismic strain along the North Anatolian Fault. (a) Schematic representation of the strain distribution in the creeping zone, which is made up of parallel zones of various strain values representative of **Fig. 8b** and **8a** from left to right, respectively, and that are represented on the right by two normal (i.e. Gaussian) distributions of the shear strain (b) Horizontal surface velocity as a function of distance from fault (black profile is for a fault locked at the surface and creeping at depth, green profile is for a fault creeping at the surface and locked at depth, red profile is for a combination of both). (c) Zoom on (b). (d) Surface strain rate as a function of distance from fault, derived from (c). (e) & (f) Geodetic horizontal creep rate profiles perpendicular to the North Anatolian Fault across Ismetpasa and Hamamli outcrops, respectively; the data (dots) and model (black lines) are taken from Cetin et al. (2014). (g) Strain rate profiles derived from creep rate models in (e) & (f). These profiles are fitted with the superposition of two normal distributions to model the shear strains and the widths of the gouge and the damage zones for Ismetpasa-Hamamli outcrops.

6. Conclusion

The quantitative evaluation of the aseismic part of the total displacement along the North Anatolian Fault provides methodological and rheological insights on strain measurements and fault mechanisms. From a methodological point of view, it has been shown that the measurement of finite strain in shear zones, which can reach very large strain values, is strongly dependent on the methodology. Methods based on the analysis of particle distribution, such as the Fry method, or length change, such as boudinage measurements, do not allow retrieving shear strains higher than 2.5 to 4, respectively. Conversely, using the variations in cleavage angle with the shear zone very large strain values up to 100 or more can be estimated, with a large uncertainty on this value. However, in both cases, evaluation of volume change is important and must be integrated in the calculation.

The relationship between strain and volume change shows that the penetrative cleavage observed in the whole NAF shear zone affecting volcanic, or analogous rocks, is a pressure solution cleavage that evolves from oblique to sub-parallel to the shear displacement. A combination of two normal (i.e. Gaussian) shear strain distributions is proposed to represent this pattern of deformation in the kilometer-width creeping zones. These zones are partitioned into parallel deformation zones with contrasting shear strain characteristics: (i) wide (10-100 m) shear zones with cleavage oblique to the shear displacement (ii) narrow (0.2-2 m) shear zones with cleavage planes sub-parallel to the shear displacement, with sub-grain shear localization.

Finally, finite shear strain characteristics evaluated from geological analyses were used in parallel with geodetic data in order to calculate the total cumulative shallow aseismic displacement that has been accommodated by creep. By modeling the present-day creep behavior, it is possible to propose a model with the two types of shear zones and evaluate the maximum width of the creeping zone. By modeling the creeping behavior since the beginning of fault sliding it is possible to calculate an aseismic part of the total 80 km displacement in the range 9 to 49% in the creeping (volcanic and analogous rocks) zone and a negligible displacement in the locked (limestone) zones, showing the crucial effect of the lithology in the seismic versus aseismic partition.

The large uncertainty in the evaluation of the NAF aseismic displacement is partly related to the difficulty of evaluating the large strain values that are associated with large shear displacement. Based on the methodology developed on thin section analysis, a promising way to improve such measurements would be to develop reliable statistical analysis of cleavage orientations in the field.

Acknowledgements: This project was funded by the European Union's Seventh Framework Programme for research, technological development and demonstration under grant agreement no. 316889 (ITN FlowTrans) and by the Norwegian Research Council grant No. 250661 'HADES' to FR. The authors wish to thank Nathaniel Findling, Valerie Magnin and Valentina Batanova for technical support with sample preparation and XRD and EPMA analytical measurements at ISTerre. The authors thank the editor, Yehuda Ben-Zion, and two reviewers for detailed comments and suggestions that improved significantly the manuscript.

References

Akbaş, B., Akdeniz, N., Aksay, A., Altun, İ., Balcı, V., Bilginer, E., Bilgiç, T., Duru, M., Ercan, T., Gedik, İ., Günay, Y., Güven, İ.H., Hakyemez, H. Y., Konak, N., Papak, İ., Pehlivan, Ş., Sevin, M., Şenel, M., Tarhan, N.,Turhan, N., Türkecan, A., Ulu, Ü., Uğuz, M.F., Yurtsever, A. and others, 2016). Turkey Geology Map General Directorate of Mineral Research and Exploration Publications. Ankara Turkey.

Andreani, M., Boullier, A. M., Gratier, J. P., 2005. Development of schistosity by dissolution-crystallization in a Californian serpentinite gouge. Journal of Structural Geology, 27, 2256-2267.

Ashby, M., Verrall, R., 1973. Diffusion-accommodated flow and superplasticity, Acta Metall. 11(2), 149-163.

1195 Armijo, R., Meyer, B., Hubert, A., Barka, A., 1999. Westward propagation of the
1196 North Anatolian fault into the northern Aegean: Timing and kinematics. Geology
1197 27, 267-270. doi:10.1130/0091-7613.
1198 Armijo, R., Meyer, B., Hubert, A., Barka, A., 2000. Westward propagation of North
1199 Anatolian fault into the northern Aegean:Timing and kinematics: Comment and
1200 Reply, Geology, 28(2), 188, doi:10.1130/0091-7613.
1201 Bilham, R., Ozener, H., Mencin, D., Dogru, A., Ergintav, S., Çakir,Z., Aytun, A.,
1202 Aktug., B., Yılmaz, O., Johnson, W., Mattioli, G.S., 2016. Surface creep on the
1203 North Anatolian Fault at Ismetpasa, Turkey, 1944-2016, J. Geophys. Res. Solid
1204 Earth, 121, 7409-7431.
1205 Bos, B., Spiers, C. J., 2002. Frictional-viscous flow of phyllosilicate-bearing fault
1206 rock: Microphysical model and implications for crustal strength profiles. J.
1207 Geophys. Res. 107, doi:10.1029/2001JB000301.
1208 Bos, B., Spiers, C. J., 2000. Effect of phyllosilicates on fluid-assisted healing of
1209 gouge-bearing faults, Earth Planet. Sci. Lett., 184(1), 199–210,
1210 doi:10.1016/S0012-821X(00)00304-6.
1211 Bürgmann, R., 2018. The geophysics, geology and mechanics of slow fault slip, Earth
1212 Planet. Sci. Lett., 495, 112-134.
1213 Çakir, Z., Akoglu, A.M., Belabbes, S., Ergintav, S., Meghraoui, M., 2005. Creeping
1214 along the Ismetpasa section of the North Anatolian fault (Western Turkey): Rate
1215 and extent from InSAR. Earth Planet. Sci. Lett. 238, 225–234.
1216 doi:10.1016/j.epsl.2005.06.044.
1217 Çakir, Z., Ergintav, S., Akoğlu, A.M., Çakmak, R., Tatar, O., Meghraoui, M., 2014.
1218 InSAR velocity field across the North Anatolian Fault (eastern Turkey):
1219 Implications for the loading and release of interseismic strain accumulation. J.
1220 Geophys. Res. Solid Earth 119, 7934–7943. doi:10.1002/2014JB011360.
1221 Carpenter, B.M., Ikari, M.J., Marone, C., 2016. Laboratory observations of time-
1222 dependent frictional strengthening and stress relaxation in natural and synthetic
1223 fault gouges. J. Geophys. Res. Solid Earth 121, 1183-1201,
1224 doi:10.1002/2015JB012136.
1225 Cetin, E., Çakir, Z., Meghraoui, M., Ergintav, S., Akoglu, A.M., 2014. Extent and
1226 distribution of aseismic slip on the Ismetpa?a segment of the North Anatolian
1227 Fault (Turkey) from Persistent Scatterer InSAR. Geochemistry, Geophys.
1228 Geosystems 15, 2883–2894. doi:10.1002/2014GC005307.
1229 Chen, K.H., Bürgmann, R., 2017. Creeping faults: Good news, bad news? Rev.
1230 Geophys. 55(2), 282-286. doi:10.1002/2017RG000565.
1231 Collettini, C., Niemeijer, A., Viti, C., Marone, C., 2009. Fault zone fabric and fault
1232 weakness, Nature, 462(7275), 907–910, doi:10.1038/nature08585.
1233 Emre, Ö., Duman, T.Y., Özalp, S., Elmacı, H., Olgun, Ş., Şaroğlu, F., 2013. Active
1234 Fault Map of Turkey with an Explanatory Text. 1:1,250,000 Scale. General
1235 Directorate of Mineral Research and Exploration (MTA), Ankara-Turkey.
1236 Emre, O., Duman, T.Y., Ozalp, S., Saroglu, F., Olgun, S., Elmaci, H., Can, T., 2016.
1237 Active fault database of Turkey. Bull. Earthq. Eng. 1–47. doi:10.1007/s10518-
1238 016-0041-2.
1239 Erslev, E., 1988. Normalized center-to-center strain analysis of packed aggregates. J.
1240 Struct. Geol. 10, 201–209. doi:10.1016/0191-8141(88)90117-4.
1241 Erslev, E., Ge, H., 1990. Least-squares center-to-center and mean object ellipse fabric
1242 analysis. J. Struct. Geol. 12, 1047–1059. doi:10.1016/0191-8141(90)90100-D.
1243 Fossen, H., Tikoff, B., 1993. The deformation matrix for simultaneous simple
1244 shearing, pure shearing and volume change, and its application to transpression-

transtension tectonics. J. Struct. Geol. doi:10.1016/0191-8141(93)90137-Y.
Fossen, H., Cavalcante, G.C.G., 2017. Shear zones – A review. Earth-Science Rev., 171, 434-455, doi:10.1016/j.earscirev.2017.05.002.
Fry, N., 1979. Random point distributions and strain measurement in rocks. Tectonophysics, 60, 89–105. doi:10.1016/0040-1951(79)90135-5.
Genier, F., Epard, J.L., 2007. The Fry method applied to an augen orthogneiss: Problems and results. J. Struct. Geol. 29, 209–224. doi:10.1016/j.jsg.2006.08.008.
Gratier, J., Dysthe, D.K., Renard, F., 2013. The role of pressure solution creep in the ductility of the Earth ' s upper crust, Advances in Geophysics. 54, 47-179, doi:10.1016/B978-0-12-380940-7.00002-0.
Gratier, J.P., Richard, J., Renard, F., Mittempergher, S., Doan, M.L., Di Toro, G., Hadizadeh, J., Boullier, a. M., 2011. Aseismic sliding of active faults by pressure solution creep: Evidence from the San Andreas Fault Observatory at Depth. Geology 39, 1131–1134. doi:10.1130/G32073.1.
Gratier, J.-P., Noiriel, C., Renard, F., 2015. Experimental evidence for rock layering development by pressure solution, Geology, 43(10), 871–874, doi:10.1130/G36713.1.
Graymer, R.W., Ponce, D.A., Phelps, G.A., Wentworth, C.M., 2005. Three-dimensional geologic map of the Hayward fault, northern California : Correlation of rock units with variations in seismicity, creep rate, and fault dip, Geology, 33, 521–524. doi:10.1130/G21435.1.
Harris, R.A., 2017. Large earthquakes and creeping faults. Rev. Geophys. 55, 169–198. doi:10.1002/2016RG000539.
Herece, E. I., and E. Akay (2003), Atlas of North Anatolian Fault, General Directorate of Mineral Research and Exploration (MTA), Ankara-Turkey.
Heilbronner, R., 2002. Analysis of bulk fabrics and microstructure variations using tesselations of autocorrelation functions. Comput. Geosci. 28, 447–455. doi:10.1016/S0098-3004(01)00088-7.
Heilbronner, R., Barrett, S., 2014. Image Analysis in Earth Sciences Microstructures and Textures of Earth Materials, Springer Science and Business Media, Berlin.
Hull, J., 1988. Thickness-displacement relationships for deformation zones 10, 431–435. doi:10.1016/0191-8141(88)90020-X.
Hussain, E., Hooper, A., Wright, T.J., Walters, R.J., Bekaert, D.P.S., 2016. Interseismic strain accumulation across the central North Anatolian Fault from iteratively unwrapped InSAR measurements. J. Geophys. Res. Solid Earth 121, 9000–9019. doi:10.1002/2016JB013108.
Imber, J., Holdsworth, R.E., Butler, C.A., Strachan, R.A., 2001. A reppraisal of the Sibson-Scholz fault model: the nature of the frictionnal to viscous (brittle-ductile) transition along a long-lived crustal-scale fault, Outer Hebrides, Scotland, Tectonics 20, 601-624.
Janssen, C., Michel, G.W., Bau, M., Lüders, V., and Mühle K., 1997. The North Anatolian Fault Zone and the Role of Fluids in Seismogenic Deformation, J. Geol., 105(3), 387–404, doi:10.1086/515934.
Jefferies, S.P., Holdsworth, R.E., Wibberley, C.A.J., Shimamoto, T., Spiers, C.J., Niemeijer, A.R., Lloyd, G.E., 2006. The nature and importance of phyllonite development in crustal-scale fault cores: an example from the Median Tectonic Line, Japan, Journal of Structural Geology, 28, 220-235.
Kaduri, M., Gratier, J.-P., Renard, F., Çakir, Z., Lasserre, C., 2017. The implications of fault zone transformation on aseismic creep: Example of the North Anatolian

Fault, Turkey. J. Geophys. Res. Solid Earth., 122, 4208–4236, doi:10.1002/2016JB013803.
Kaneko, Y., Fialko, Y., Sandwell, D.T., Tong, X., Furuya, M., 2013. Interseismic deformation and creep along the central section of the North Anatolian Fault (Turkey): InSAR observations and implications for rate-and-state friction properties. J. Geophys. Res. Solid Earth 118, 316–331. doi:10.1029/2012JB009661.
Karmakar, S., Lemaître, A., Lerner, E., Procaccia, I., 2010. Predicting Plastic Flow Events in Athermal Shear-Strained Amorphous Solids. Phys. Rev. Lett. 104, 215502. doi:10.1103/PhysRevLett.104.215502
Lockner, D., Morrow, C., Moore, D., Hickman, S., 2011. Low strength of deep San Andreas fault gouge from SAFOD core. Nature 472, 82–85. doi:10.1038/nature09927.
Mavko, G.M., 1981. Mechanics of Motion on Major Faults. Annu. Rev. Earth Planet. Sci. 9, 81–111. doi:10.1146/annurev.ea.09.050181.000501
Mulchrone, K.F., 2013. Fitting the void: Data boundaries, point distributions and strain analysis. J. Struct. Geol. 46, 22–33. doi:10.1016/j.jsg.2012.10.011
Okada, Y., 1985. Surface deformation due to shear and tensile faults in a half-space. Bulletin of the seismological society of America, 75(4), 1135-1154.
Pennacchioni, G., 2005. Control of the geometry of precursor brittle structures on the type of ductile shear zone in the Adamello tonalites, Southern Alps (Italy) 27, 627–644. doi:10.1016/j.jsg.2004.11.008.
van der Pluijm, B.A., Marshak, S., 2010. Earth Structures: An Introduction to Structural Geology and Tectonics, 2nd Edition. W.W. Norton Company, New York.
Ramsay, J.G., 1980. Shear zone geometry: A review. J. Struct. Geol. 2, 83–99. doi:10.1016/0191-8141(80)90038-3.
Ramsay, J.G., 1967. Folding and fracturing of rocks. McGraw-Hill, New York.
Ramsay, J.G., Graham, R.H., 1970. Strain variation in shear belts. Can. J. Earth Sci. 7, 786–813. doi:10.1139/e70-078.
Reilinger, R. et al., 2006. GPS constraints on continental deformation in the Africa-Arabia-Eurasia continental collision zone and implications for the dynamics of plate interactions, J. Geophys. Res. Solid Earth, 111(5), 1–26, doi:10.1029/2005JB004051.
Renard, F., Dysthe, D.K., Feder, Bjørlykke, K., Jamtveit B., 2001. Enhanced pressure solution creep rates induced by clay particles: Experimental evidence in salt aggregates, Geophys. Res. Lett., 28(7), 1295–1298, doi:10.1029/2000GL012394.
Richard, J., Gratier, J.-P., Doan, M., Boullier, A., Renard, F., 2014. Rock and mineral transformations in a fault zone leading to permanent creep: Interactions between brittle and viscous mechanisms in the San Andreas Fault. J. Geophys. Res. Solid Earth 119, 8132–8153. doi:10.1002/2014JB011489.
Rousset, B., Jolivet, R., Simons, M., Lasserre, C., Riel, B., Milillo, P., Çakir, Z., Renard, F., 2016. An aseismic slip transient on the North Anatolian Fault, Geophys. Res. Lett., 43(7), 3254–3262, doi:10.1002/2016GL068250.
Samuelson, J., Spiers, C.J., 2012. Fault friction and slip stability not affected by CO_2 storage: Evidence from short-term laboratory experiments on North Sea reservoir sandstones and caprocks. Int. J. Greenh. Gas Control, 11, 78–90. doi:10.1016/j.ijggc.2012.09.018.
Savage, J.C., Burford, R.O., 1973. Geodetic determination of relative plate motion in central California. J. Geophys. Res. 78, 832–845. doi:10.1029/JB078i005p00832

1345 Scholz, C.H., 2002. The Mechanics of Earthquake Faulting, 2nd Edition. Cambridge
1346 University Press, Boston.
1347 Şengör, A. M. C., O. Tuysuz, C. Imren, M. Sakinc, H. Eyidogan, N. Gorur, X.
1348 LePichon, and C. Rangin (2004), The North Anatolian fault: A new look, Annu.
1349 Rev. Earth Planet. Sci., 33, 1–75.
1350 Sone, H., Shimamoto, T., Moore, D.E., 2012. Frictional properties of saponite-rich
1351 gouge from a serpentinite-bearing fault zone along the Gokasho-Arashima
1352 Tectonic Line, central Japan. J. Struct. Geol. 38, 172–182.
1353 doi:10.1016/j.jsg.2011.09.007.
1354 Stein, R.S., Barka, A., Dieterich, J.H., 1997. Progressive failure on the North
1355 Anatolian fault since 1939 by earthquake stress triggering. Geophys. J. Int. 128,
1356 594–604. doi:10.1111/j.1365-246X.1997.tb05321.x.
1357 Stewart, M.A., Holdsworth, R.E., and Strachan, R.A., 2000. Deformation processes
1358 and weakening mechanisms within the frictional-viscous transition zone of major
1359 crustal faults: insights from the Great Glen Fault zone, Scotland, Journal of
1360 Structural Geology, 22, 543-560.
1361 Toussaint, R., E. Aharonov, D. Koehn, J-P. Gratier, M. Ebner, P. Baud, A. Rolland, F.
1362 Renard, 2018, Stylolites : a review, Journal of Structural Geology, 114, 163-195,
1363 doi:101016/j.jsg.2018.05.003.
1364 Thomas, M.Y., Avouac, J.-P., Gratier, J.-P., Lee, J.-C., 2014. Lithological control on
1365 the deformation mechanism and the mode of fault slip on the Longitudinal
1366 Valley Fault, Taiwan. Tectonophysics 632, 48–63.
1367 doi:10.1016/j.tecto.2014.05.038.
1368 Vitale, S., Mazzoli, S., 2008. Heterogeneous shear zone evolution : The role of shear
1369 strain hardening / softening. J. Struct. Geol. 30, 1383–1395.
1370 doi:10.1016/j.jsg.2008.07.006.
1371 Zubtsov, S., Renard, F., Gratier, J.P., Guiguet, R., Dysthe, D.K., Traskine, V., 2004.
1372 Experimental pressure solution compaction of synthetic halite/calcite aggregates.
1373 Tectonophysics 385, 45–57. doi:10.1016/j.tecto.2004.04.016.